THESIS

A LOW-COST MONITOR FOR SIMULTANEOUS MEASUREMENT OF FINE PARTICULATE MATTER AND AEROSOL OPTICAL DEPTH

Submitted by

Eric Wendt

Department of Mechanical Engineering

In partial fulfillment of the requirements

For the Degree of Master of Science

Colorado State University

Fort Collins, Colorado

Spring 2018

Master's Committee:

Advisor: John Volckens

Shantanu Jathar
Azer Yalin
Jeffrey Pierce

ABSTRACT

A LOW-COST MONITOR FOR SIMULTANEOUS MEASUREMENT OF FINE PARTICULATE MATTER AND AEROSOL OPTICAL DEPTH

Exposure to airborne particulate matter with diameters less than 2.5 μm ($PM_{2.5}$) is a leading cause of death and disease globally. In addition to affecting health, $PM_{2.5}$ affects climate and atmospheric visibility. NASA currently uses satellite imaging technology to measure particulate matter air pollution across the world. Satellite image data are used to derive aerosol optical depth (AOD), which is the extinction of light in the atmospheric column. Although AOD data are often used to estimate surface $PM_{2.5}$ concentration, there is considerable uncertainty associated with the relationship between satellite-derived AOD and ground-level $PM_{2.5}$. Instruments known as Sun photometers can measure AOD from the Earth's surface and are often used for validation and calibration of satellite data. Reference-grade Sun photometers generally do not have co-located $PM_{2.5}$ measurements and are too expensive to deploy in large numbers. The objective of this work was to develop an inexpensive and compact integrated $PM_{2.5}$ mass and AOD sampler known as the Solar-Powered Aerosol Reference Calibrator (SPARC). $PM_{2.5}$ is sampled using an ultrasonic pumping system, a size-selective cyclone separator, and a filter. Filter measurements can be used to correct the output from a low-cost direct-reading $PM_{2.5}$ sensor housed within the SPARC. AOD is measured using optically filtered photodiodes at four discrete wavelengths. A suite of integrated sensors enable time-resolved measurement of key metadata including location, altitude, temperature, barometric pressure, relative humidity, solar incidence angle and spatial orientation. The AOD sensors were calibrated relative to a reference monitor in the Aerosol Robotics Network (AERONET). Field validation studies revealed close agreement for AOD values measured between co-located SPARC and AERONET monitors and for $PM_{2.5}$ mass measured between co-located SPARC and EPA Federal Reference Method (FRM) monitors. These field validation results for this novel monitor demonstrate that AOD and PM2.5 can be accurately measured for the evaluation of AOD:$PM_{2.5}$ ratios.

ACKNOWLEDGEMENTS

I would like to thank my advisor John Volckens for his vision, guidance and support through this project. I would also like to thank Casey Quinn, Dan Miller-Lionberg and Todd Hochwitz. This technology would not have come into being without their previous efforts and continual support. I am grateful for the efforts of my fellow members of the Citizen Enabled Aerosol Measurements for Satellites (CEAMS) team including Jessica Tryner, Bonne Hotmann, Christian L'Orange, John Mehaffy, David Brooks, Marilee Long and Lizette van Zyl. A special thanks is due to my sister Caroline Wendt for her selfless contributions to graphic design and data collection for this project. I also thank Michele Kuester of Digital Globe and Janae Csavina of NEON for allowing me to take measurements at their AERONET sites.

I thank professors John Volckens, Jeff Pierce, Shantanu Jathar and Azer Yalin for being a part of my committee and for their individual contributions to the CEAMS effort.

This work was supported by the National Aeronautics and Space Administration under Agreement No. NNX17AF94A.

TABLE OF CONTENTS

LIST OF NOMENCLATURE

$PM_{2.5}$	Particulate Matter Less than 2.5 Microns in Diameter
AOD	Aerosol Optical Depth
AERONET	Aerosol Robotics Network
FWHM	Full-Width Half-Maximum
FRM	Federal Reference Method
FEM	Federal Equivalent Method
UPAS	Ultrasonic Personal Aerosol Sampler
SPARC	Solar-Powered Aerosol Reference Calibrator
LED	Light Emitting Diode
VCSEL	Vertical Cavity Surface Emitting Laser
CAD	Computer Animated Design
I2C	Inter-Integrated Circuit
UART	Universal Asynchronous Receiver-Transmitter
NREL	National Renewable Energy Laboratory
UNC	Unified National Coarse
PCB	Printed Circuit Board
SOC	State of Charge
IoT	Internet of Things

CHAPTER 1. INTRODUCTION

1.1 Particulate matter, health, and the environment

Particulate matter less than 2.5 μm in diameter ($PM_{2.5}$) is a leading cause of premature death and disease globally [1]. When inhaled, $PM_{2.5}$ can penetrate deep into the lungs, which can cause long and short term health problems [2, 3]. Exposure to ambient air pollution is currently ranked as the 6th leading risk factor for premature death and disease globally [1]. In 2013, 2.9 million deaths were attributed to $PM_{2.5}$ from both anthropogenic and biogenic sources [1].

In addition to public health decrements, particulate matter contributes to the visual degradation of the atmosphere, and also impacts the climate [4]. The presence of haze due to particulate matter reduces visibility and diminishes natural color. This is of concern in National Parks and other tourist destinations where visibility degradation may diminish the local economy and aesthetic. Ambient particulate matter also affects the radiative budget of Earth's atmosphere. Particles scatter and absorb Solar radiation and infrared thermal radiation from the Earth's surface [4]. These phenomena lead to both cooling and warming effects that are not completely understood [4].

1.2 Measurement of $PM_{2.5}$ using satellites

Satellites equipped with imaging instruments can measure a quantity known as aerosol optical depth (AOD): a dimensionless measure of light extinction by aerosols in the atmospheric column. Measurements of AOD are used to estimate surface-level $PM_{2.5}$ concentrations [5-7]. Such satellite-based estimates of $PM_{2.5}$ have made considerable impact in helping quantify air pollution levels in areas where no surface monitoring occurs. There is growing interest in defining the precise relationship between AOD and $PM_{2.5}$ concentration, which has been modeled as follows [8]:

$$PM_{2.5} = \eta * AOD \quad (1)$$

where η is a conversion factor between $PM_{2.5}$ and AOD. If η is known, satellite AOD measurements can be used to infer surface particulate matter concentration. However, this conversion is not well characterized [8]. Additionally, satellite measurements are suspect to measurement error [4, 8-12]. Instruments known as

Sun photometers are used to validate satellite measurements. When used alongside $PM_{2.5}$ samplers, Sun photometers aid in deriving empirical relations between AOD and $PM_{2.5}$ concentration [8].

1.3 Sun photometry

Sun photometers utilize photodetectors to measure incident sunlight directly. In conjunction with the Beer-Lambert-Bouger, aerosol optical depth, τ_a, may be calculated from this measurement per the following equation:

$$\tau_a(\lambda) = \frac{1}{m}\left(\ln\left(\frac{V_0}{R^2}\right) - ln(V)\right) - \tau_R(\lambda, p) - \tau_{O3} \quad (2)$$

where, m is the relative optical air mass factor that accounts for deviations from overhead sunlight, R is the earth-sun distance in astronomical units (AU), V is the voltage read by the light detector, τ_R accounts for Rayleigh scattering by air molecules, p is the pressure, λ is the wavelength, τ_{O3} accounts for ozone absorbtion, and V_0 is the voltage produced by light at the top of the atmosphere and is referred to as the extraterrestrial constant [4, 9]. The most common method to find V_0 is the Langley plot method [13]. By combining the aerosol and Rayleigh components into total optical depth and rearranging Eq. 2, the following equation (used for a Langley plot) is derived:

$$ln(V) = ln\frac{V_0}{R^2} - \tau_a(\lambda) * m \quad (3)$$

During a Langley calibration, voltage measurements are taken as the air mass factor changes over the course of a day. The slope of the line gives total optical depth and the intercept at $m = 0$ gives the constant V_0.

Sun photometers equipped to measure at multiple wavelengths can provide data useful for evaluating aerosol size distributions [14]. When AOD is measured at multiple wavelengths, AOD for non-measured wavelengths may be inferred using the following relation [15]:

$$\tau_a(\lambda) = \tau_{a0} * (\lambda_0) * (\frac{\lambda}{\lambda_0})^{-\alpha} \quad (4)$$

where α is the Ångström coefficient, λ_0 is a wavelength measured by photometer, λ is the new wavelength land τ_{a0} is the measured AOD from the photometer. The Ångström coefficient varies depending on the

aerosol size distribution; larger aerosols generally give rise to lower values for α compared with smaller aerosols [4].

Equation 2 was developed under the assumption that the photometer measures the intensity of monochromatic incident light [9]. Because the Sun is a polychromatic emitter, Sun photometers feature light detectors of narrow spectral bandwidth [16]. Light detectors with full-width half-maximum (FWHM) spectral bandwidths of 15 nm or less can be approximated as monochromatic [9]. This requirement precludes the use of inexpensive photodiodes as light detectors because of their wide spectral bandpass. Standard reference instruments, such as the CE318 (Cimel Electronique SAS, Paris, France) used in the Aerosol Robotics Network (AERONET), often include photodiodes fitted with optical interference filters to achieve monochromatic detection [11]. However, these filters can be cost prohibitive at ~$100 per device and tend to degrade over time, requiring frequent recalibration [10, 11]. The high cost and high maintenance requirements has often disqualified the use of expensive interference filter Sun photometers in large-scale validation studies and in locations where adequate capital and trained operators are lacking.

A durable and cost-effective hand-held Sun photometer was presented by Mims (1992) that utilized light emitting diodes (LEDs) as inexpensive, sturdy, and spectrally selective photodetectors in a handheld device [17]. Although LEDs are significantly cheaper than optical interference filters, they are not as spectrally selective and they are also sensitive to changes in temperature [9]. LED Sun photometers have been operated, for satellite validation work, by secondary school students as part of the Global Learning and Observations to Benefit the Environment (GLOBE) program [9, 12].

1.4 Measurement of $PM_{2.5}$ Mass at the Earth's Surface

The U.S. Environmental Protection Agency regulates ambient concentrations of $PM_{2.5}$ mass [18]. The EPA has designated a list of Federal Reference Methods (FRMs) and Federal Equivalent Methods (FEMs) that are used to monitor $PM_{2.5}$ [19]. FRMs adhere to a set of design and performance characteristics specified by the EPA [18]. Designation as an FRM requires that there be no significant deviations between the FRM design specifications and the monitor in question [18]. If there are significant design deviations, a monitor may qualify to be an FEM based on a series of rigorous comparison testing with FRMs [18]. The

deployment prospects of FRM and FEM monitors are limited by their high cost ($10,000-$30,000) and the need for trained operators [20].

1.5 Objectives

The objective of this work was to develop a user-friendly and low-cost aerosol sampler capable of reference quality $PM_{2.5}$ and AOD measurements. This work leveraged new, low-cost electronics technology to address cost, performance, and usability issues associated with the prior art of AOD and $PM_{2.5}$ measurement. AOD measurement technology was integrated with a gravimetric Ultrasonic Personal Aerosol Sampler (UPAS) developed at Colorado State University [21]. The resultant device, Solar-Powered Aerosol Reference Calibrator (SPARC), is capable of simultaneous sunlight and mass-based particulate matter measurement. SPARC measurements were independently validated against reference monitors. The unique combination of AOD, gravimetric filter $PM_{2.5}$, and real-time $PM_{2.5}$ sampling on a compact, low-cost, and user-friendly platform, make the SPARC amenable to large-scale deployment in spatially dense sampling networks. The long-term aim of this work is to establish several of these networks to monitor pollution exposure within metropolitan areas and provide a high-resolution data set for evaluating the relationship between AOD and $PM_{2.5}$.

CHAPTER 2. MATERIALS AND METHODS

2.1 Instrument Design

SPARC development was based on the existing hardware and software architecture of the UPAS sampler, which was developed and validated previously [21, 22]. The wearable UPAS was designed primarily to measure personal exposure in indoor and work environments [21]. The scientific goals of the SPARC development dictated the UPAS be modified for outdoor and primarily stationary sampling of both $PM_{2.5}$ and AOD. Notable modifications include: a) Additional hardware to support AOD measurement capability; b) A new weather-resistant housing; c) A larger battery and a solar panel for extended battery life; d) Software updates for simultaneous $PM_{2.5}$ and AOD sampling.

The first step in the design process was light detector selection. Sensing options from previous studies that were explored include filtered photodiodes (Intor Inc., Socorro, NM, USA) and light emitting diodes (LEDs) (Lighthouse LED A-FSMUBC12, WA, USA) [17, 23]. Novel technology considered included vertical cavity surface emitting lasers (VCSELs) (Vixar Inc. I0-0680M-0000-KP01, Plymouth, MN, USA) acting as detectors [24]. These detector options were evaluated according to cost, variety of available center wavelengths, and spectral bandwidths FWHM. Filtered photodiode and VCSEL FWHM bandwidths were tested using a tunable dye laser (Sirah Lasertechnik Allegro, Grevenbroich, Germany). LED response spectra extended outside the scanning range of the tunable dye laser and were tested using a tunable light source (Optometrics TLS-25M, Littleton, MA, USA). For each test, the laser was scanned across a pre-selected wavelength range. The laser beam was directed to the active area of the light detectors via a series of lenses. Four specimens were tested for each detector type. Typical spectral response plots for VCSELs, LEDs, and filtered photodiodes are depicted in Figure 2-1.

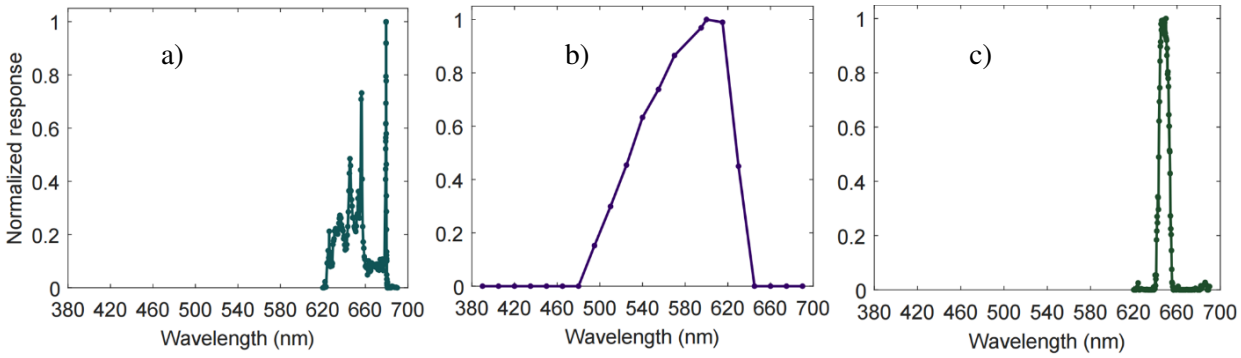

Figure 2-1. Spectral response curves for (a) 680 nm VCSEL, (b) 620 nm LED and (c) 680 nm filtered photodiode. The vertical axis gives the detector response normalized with respect to dye laser power and maximum detector signal output.

The FWHM bandwidth of VCSELs acting in reverse was less than 1 nm centered at 680nm. However, the VCSELs exhibited several response peaks at wavelengths below 680 nm. The average FWHM bandwidth for LEDs was approximately 100 nm centered at 600 nm. Previous studies have reported LED detection FWHM bandwidths of between 25 nm and 75 nm [9, 25]. The relatively broad spectral bandwidths of LEDs has prompted the development of compensation algorithms to mitigate errors [9]. The measured filtered photodiode behavior approximated that reported by the manufacturer. The datasheet specified a FWHM bandwidth of 10 nm and a center wavelength of 680 nm. The measured values were within 5 nm of the expected values, measured at FWHM. Cost was also considered during the evaluation of light detectors. VCSELs were the most expensive per unit at $75.00, followed by filtered photodiodes at $28.50, and LEDs at $0.21.

Filtered photodiodes were selected for use in the SPARC due to their sufficiently narrow spectral response bandwidth and relatively low cost. Filtered photodiodes are also commercially available at center wavelength from 400 nm to 1000 nm in increments of approximately 10 nm. No other detector option offered as broad of a selection. VCSELs were cost prohibitive and exhibited multiple undesirable response peaks. LEDs were the most inexpensive option to be evaluated but were not selected due to their broad spectral response bandwidth.

The AOD measurement system was developed independently and iteratively prior to integration with the UPAS as shown in Figure 2-2. Initial prototyping was carried out using low-cost electronics interfaced with an open-sourced, Arduino® development board. This circuit included an LED standing in as the sunlight detector. The output signal of the LED was amplified using a transimpedence amplifier circuit and interfaced with the Arduino® using a 16-bit analog to digital converter.

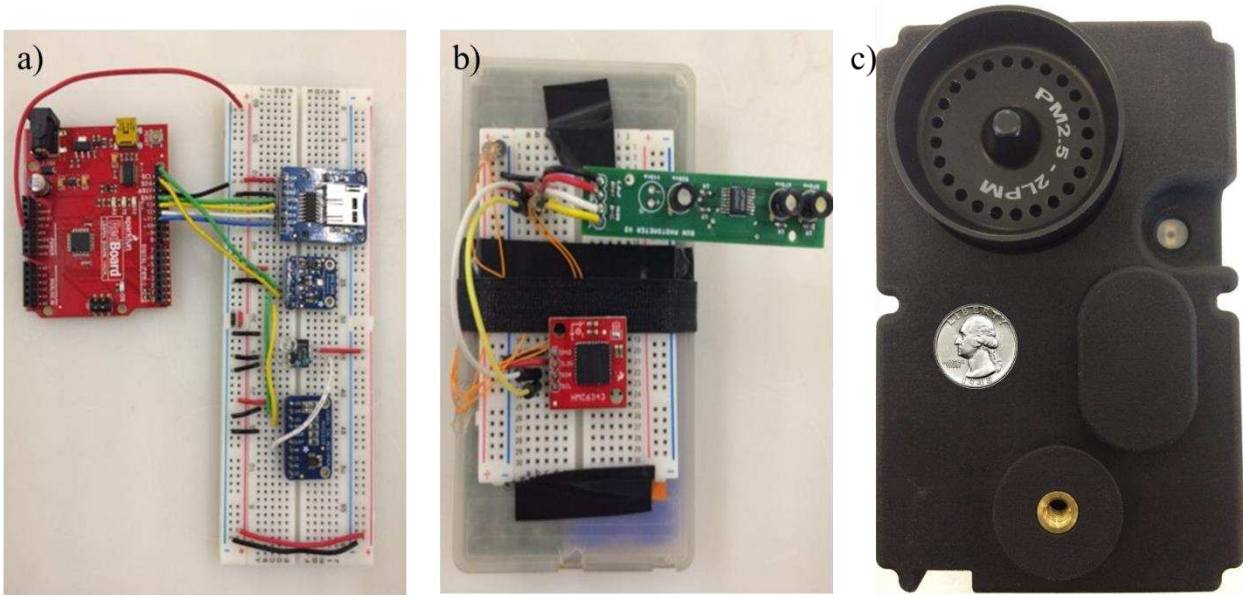

Figure 2-2. (a) Arduino breadboard LED photometer circuit (b) Custom AOD circuit board with filtered photodiodes wired to a UPAS unit (c) Fully integrated SPARC housing containing all AOD and $PM_{2.5}$ mass sampling hardware.

The next phase in the development process was the integration of Sun photometer technology with the UPAS gravimetric sampler. A preliminary printed circuit board containing AOD measurement instrumentation was designed using Autodesk® EAGLE (Figure 2-2b). This board contained pads for 4 filtered photodiodes (Intor), a quad operational amplifier with low leakage current (Linear Technology LTC 6242) and a 16-bit analog to digital converter (Texas Instruments ADS1115, Dallas, Texas, USA). Photodiode wavelengths of 440 nm, 520 nm, 680 nm, and 870 nm were selected to avoid molecular absorption bands, match those used by AERONET, and to facilitate aerosol size distribution evaluation [14]. A final iteration of the board design added a solar incidence sensor (Solar MEMS NANO-ISS5,

Seville, Spain) and a Wi-Fi module (Espressif Systems ESP8266, Shanghai, China). The board is interfaced with the primary UPAS motherboard via I2C and UART communication. The AOD sensor firmware was adjusted to be compatible with the integrated microcontroller (mbed™ ARM® Ltd., Cambridge, UK) that controls the gravimetric sampling. The housing was designed using computer-aided design software (SolidWorks® ANSYS, Inc., Canonsburg, PA, USA) and built using stereolithographic printing (Figure 2-2c). A CAD rendering highlighting key internal and structural components of the SPARC is provided in Figure 2-3. A direct-reading particulate matter sensor (Plantower PMS5003, Beijing, China) is integrated into the sampler housing (Figure 2-3). The PMS5003 includes a fan that draws aerosol through the path of a laser diode and a photodetector. Particulate matter concentrations are evaluated, by a microprocessor embedded in the PMS5003 using Mie theory, and accessed via serial communication [26]. The SPARC housing includes a sealed inlet and outlet for flow through the sensor.

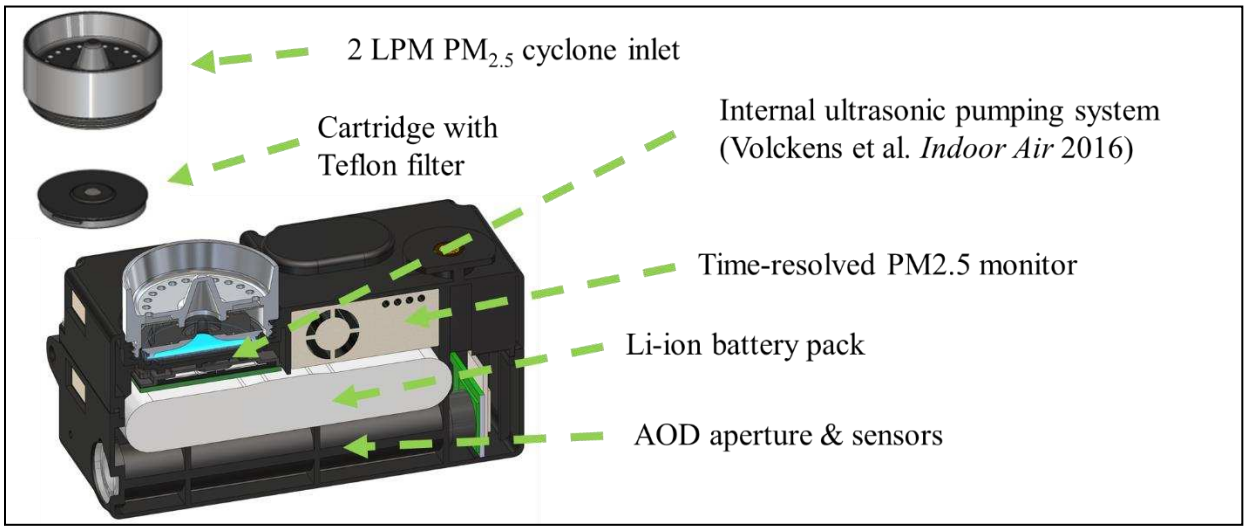

Figure 2-3. CAD rendering of key internal SPARC components used for $PM_{2.5}$ and AOD sampling.

The housing design includes 4 tubes that limit the field of view of the light detectors. A CAD rendering highlighting this portion of the housing is provided in Figure 2-4.

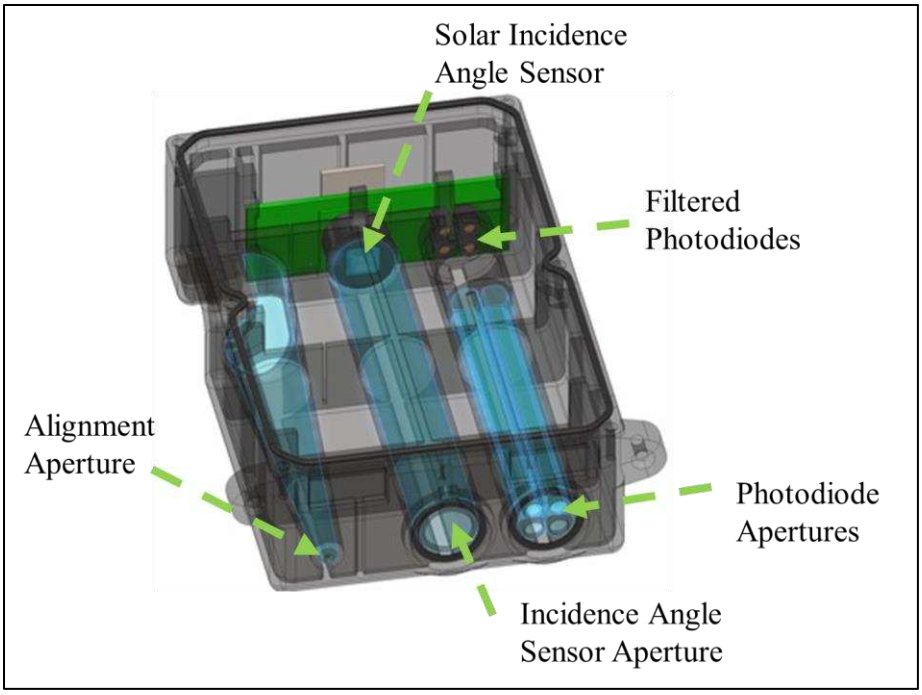

Figure 2-4. CAD rendering of SPARC AOD measurement system including the light apertures and electronic hardware components. Light blue shading indicates a hollow region for light transmission; black and green shading indicate the housing and AOD circuit board, respectively.

Light enters through 5mm diameter apertures on the top surface of the housing and subsequently passes through 112mm long tubes to the active area the filtered photodiodes. These proportions yield a viewing angle of 2.56 degrees per sensor. A narrow viewing angle is required to mitigate errors caused by forward scattered sunlight entering the field of view of the detector [27]. The housing includes two sockets with ¼ - 20 Unified National Coarse (UNC) threads, which allow the SPARC to be easily mounted to standard camera tripods. The SPARC battery is charged via a barrel plug port on the side of the housing; this plug also accepts power from the solar panel. The plug is water tight when the panel cable is attached to the barrel port. This port can be interfaced with an external battery, wall charger or solar panel (Voltaic® 3.5W). The internal SPARC battery is a 3.6, 20.1Ah custom battery pack comprised of six 18650 lithium ion cells (Panasonic NCR18650B). The solar panel is mounted to the exterior housing using magnets adhered to opposing surfaces on the panel and SPARC housing. The panel easily can be attached and detached from the housing. A SPARC with a solar panel attached is shown in Figure 2-5.

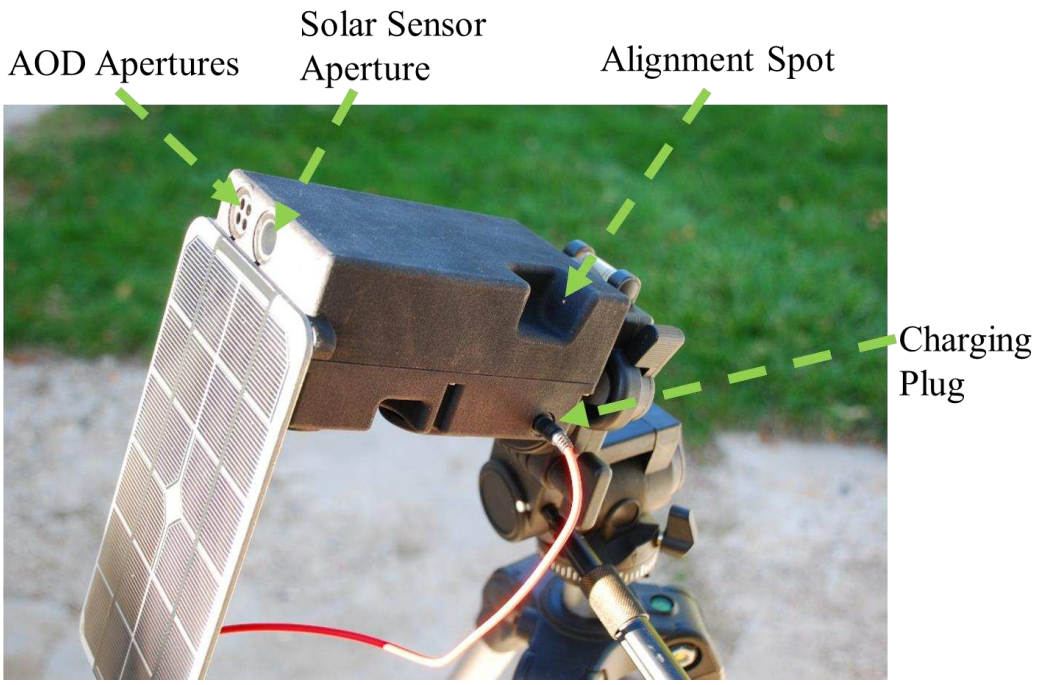

Figure 2-5. SPARC with a solar panel magnetically attached.

The sampler measures 9.0 cm W x 14.1 cm H x 6.7 cm L and is 0.64 kg. The housing is weather-resistant when mounted in its intended orientation—with the $PM_{2.5}$ inlet facing the ground and the AOD apertures pointed toward the Sun (Figure 2-5). An O-ring seal prevents leakage through the seam of the housing halves and float glass windows sealed with foam adhesive protect the optical apertures. In a durability study, five SPARC units were mounted and activated for two days, which included intermittent rain and snow. At the end of the test, no units showed evidence of damage or intrusion from either ice or water.

A cost of goods summary for notable components is provided in Table 2. The total cost of goods of the SPARC is less than $1,100. This tabulation is based on the preliminary production run of 24 units. Costs of these goods—particularly circuit boards and mechanical components—are reduced at higher quantities. The costs of electronic components not explicitly mentioned in Table 2 are included in the costs of the Printed Circuit Boards (PCBs).

Table 1. SPARC Cost of Goods Summary

Component	Manufacturer	Part Number	Cost
PCBs	NOVA Engineering	Custom Parts	$475
440 nm Filtered Photodiode	Intor	Unavailable	$28
520 nm Filtered Photodiode	Intor	Unavailable	$26
680 nm Filtered Photodiode	Intor	Unavailable	$26
870 nm Filtered Photodiode	Intor	Unavailable	$28
Direct-Reading $PM_{2.5}$ Sensor	Plantower	PMS5003	$15
Solar Alignment Sensor	Solar MEMS	NANO-ISS5	$45
SPARC Housing	Xometry	Custom Part	$130
Cyclone and Inlet	Synergy Core	Custom Part	$74
3.5 W Solar Panel	Voltaic	Unavailable	$35
Battery Pack	Battery Space	CU-JAS380	$94
Misc. Housing Components	N/A	N/A	$44
Total Costs			**$1020**

2.2 AOD Calculation Algorithm

Proper alignment of the Sun photometer and determination of the relative optical air mass factor (m) require accurate calculations (or measurements) the Sun location relative to magnetic north and the horizon. The angular location of the Sun relative to magnetic north is defined by the azimuth angle, which is measured between 0 and 360 degrees eastward from north. The angular location of the Sun relative to the horizon is defined by the elevation angle, which is measured vertically from the horizon. The zenith angle defines the position of the Sun relative to the axis normal to the Earth's surface and is related to the elevation angle by the following relationship:

$$\theta = 90° - e \quad (5)$$

where θ is the zenith angle and e is the elevation angle (both in degree units). The zenith angle quantifies the deviation in measurement from direct overhead sunlight and is particularly relevant to Sun photometry. As the zenith angle increases, incident sunlight passes through a greater distance of atmosphere, leading to increased attenuation by aerosols [4].

The National Renewable Energy Laboratory (NREL) published a solar position algorithm to calculate azimuth, elevation and zenith angles at uncertainties equal to ± 0.0003 as a function of location, time and for years between 2000 and 6000 [28]. The algorithm described in the NREL publication was implemented as a C++ microcontroller code to automate solar calculations for the SPARC. This code was verified against results from the online solar position calculator developed by NREL.

Prior to applying Equation 1 to calculate AOD, the relative optical air mass factor (m), the Rayleigh optical depth (τ_R) and the Earth-Sun distance (R) must be determined in accordance with the measurement location, time, pressure and temperature. Software was written to automate calculations and minimize user input during the process.

The AOD calculation software includes the Sun position algorithm previously described. The Earth-Sun distance is calculated directly by the solar position algorithm and stored for later use by the AOD software. The relative optical air mass factor is then calculated in terms of the solar zenith angle, θ, as follows [29]:

$$m = \frac{1.002432*cos^2(\theta)+0.148386*\cos(\theta)+0.0096467}{cos^3(\theta)+0.149864*cos^2(\theta)+0.0102963*\cos(\theta)+0.000303978} \quad (6)$$

The contributions of Rayleigh scattering and Ozone absorption to total optical depth are often substantial and must be subtracted from total optical depth for accurate AOD measurements [30]. Rayleigh optical depth is inversely proportional to the fourth power of wavelength, making accurate quantification especially important for the 440 nm and 520 nm channels on the SPARC. When aerosol concentrations are low, the Rayleigh component of total optical depth can exceed AOD by an order of magnitude [30]. The SPARC algorithm incorporates absorption due to CO_2—in addition to the more abundant constituents of air—for greater accuracy at wavelength in or near the UV spectrum [30]. Rayleigh optical depth is calculated based on wavelength and ambient pressure measured by an on-board pressure sensor (Bosch Sensortec BMP 280, Kusterdingen, Germany). For example, at standard pressure (1013.25 mbar) and a CO_2 concentration of 360 ppm, the algorithm predicts Rayleigh optical depths of 0.24, 0.12, 0.041 and 0.015 at 440 nm, 520 nm, 680 nm and 870 nm, respectively [30].

The SPARC's 520 nm and 680 nm channels lay within the Chappuis ozone absorption band (450 nm – 850 nm). The effect of ozone absorption on total optical depth can become significant when AOD is low, dictating compensation as expressed in Equation 2. A temporal and spatial sinusoidal model presented by van Heuklon (1978) is used to estimate ozone concentrations in Dobson Units (DU) based on the location and time of the measurement [31]. This value is then converted into atm-cm by dividing by 1000 and multiplied by the wavelength-dependent absorption coefficient for ozone to determine the ozone optical depth [32].

Equation 1 is then applied to calculate the total optical depth using sensor inputs and the calculations described above. AOD, temperature, pressure, relative humidity, time, location, and battery status are then stored on an accessible MicroSD card (Molex 5031821852, Lisle, IL, USA). All calculation software was developed on an online, open-source platform (mbed™; ARM® Ltd.) and is executed by the on-board microcontroller (STMicroelectronics STM32L152RE, Geneva, Switzerland).

2.3 User Operation and Measurement Procedure

The SPARC was designed to be operated by individuals without a background in aerosol sampling but have an interest in air pollution and citizen science. Care was taken to minimize the complexity of the measurement process. For this reason, a smartphone application was developed that guides the user through the measurement process in a series of steps as illustrated in Figure 2-6. The application was developed as part of a preliminary citizen science study called Citizen Enabled Aerosol Measurements for Satellites (CEAMS) at Colorado State University.

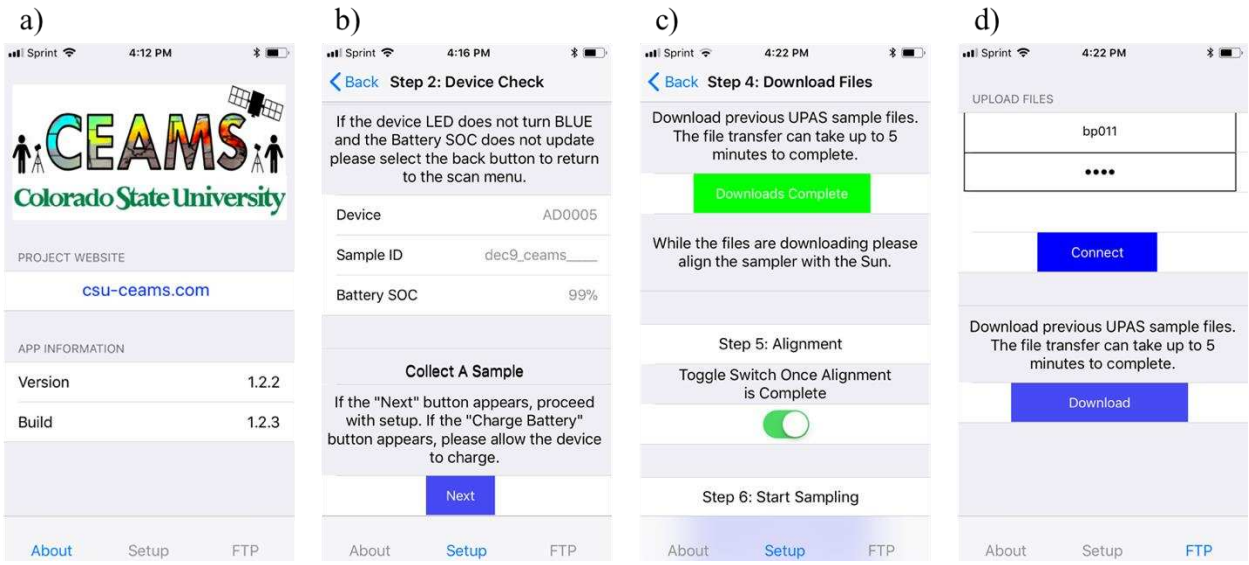

Figure 2-6. Smartphone app screen shots summarizing the key steps in the SPARC setup process: (a) Information and website link; (b) Quality assurance check; (c) Data download and alignment check; (d) file upload using standard file transfer protocol.

Items needed to complete a SPARC measurement include a SPARC unit, a filter cartridge loaded with a pre-weighed air-sampling filter, a smartphone with the setup app, and a commercial tripod or alternative mount. The application opens to an informational page that links to the CEAMS project website (Figure 2-6a). From this page, the operator selects "Setup" and connects their smartphone or tablet to the SPARC sampler over Bluetooth®. Once connection is achieved, a quality assurance page opens that displays the unit number, sample ID, and battery State of Charge (SOC) (Figure 2-6b). If the battery SOC is above 80%, the operator may proceed to the next stage in the setup by pressing the "next" button at the bottom of the page. If the SOC is below 80%, the app will prompt the operator to charge the unit before proceeding. The application then accesses the operator's phone camera and scans for a QR code adhered to the bottom of the filter cartridge (step not pictured). Once the unique cartridge ID number is recognized and saved, the operator loads the cartridge into the sampler and screws the cyclone inlet into place. The application then prompts the user to download any previous log files over Bluetooth® on to the phone (Figure 2-6c). While the files are being downloaded, the operator is encouraged to fix the SPARC to a tripod and align the AOD sensors with the sun. The alignment process is aided by an integrated pinhole and target apparatus, which

is geometrically aligned with the filtered photodiodes. The 1mm diameter pinhole projects a sunspot onto a surface on the side of the housing opposite the inlet. The operator adjusts the sampler orientation on the tripod until the sunspot is projected onto a small target, which is axially aligned with the pinhole. The alignment apparatus is illustrated in Figure 2-7.

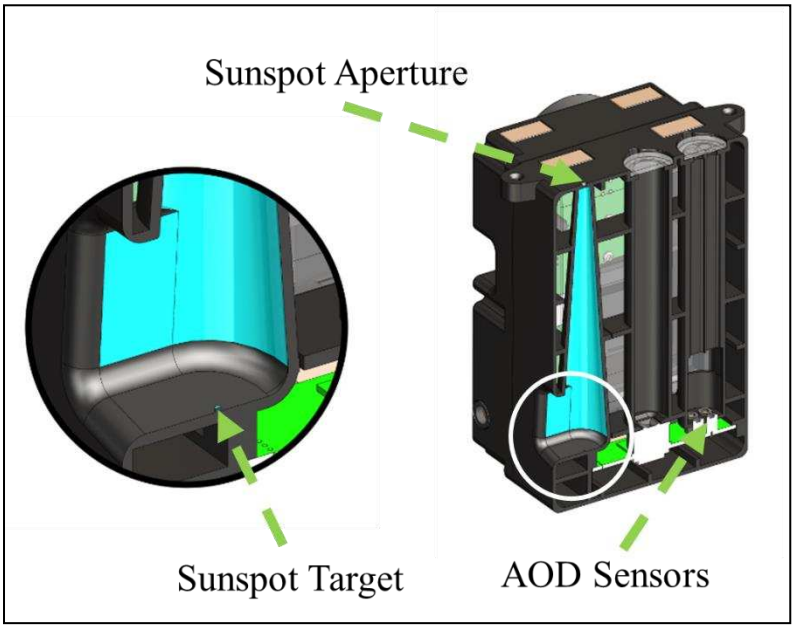

Figure 2-7. Graphical illustration of the SPARC solar alignment apparatus. The internal surface of the alignment cone, the pinhole aperture, and the sunspot target are highlighted in light blue.

Once the filter cartridge is loaded and the SPARC is aligned with the sun, the operator presses a "start" button below the alignment check icon on the application page. The SPARC then records an instantaneous AOD measurement and begins sampling air at 2L/min. Flow-controlled air sampling continues for 48.25 hours before the SPARC automatically shuts off. The SPARC maintains a fixed orientation on a tripod for the entire sampling duration—barring any unintended movements. The SPARC samples AOD 3 times over the specified 48-hr sampling period: immediately after the sample starts, 24 hours into the sample, and 48 hours into the sample. To partially mitigate errors caused by day-to-day changes in the Sun's position, the SPARC begins measuring AOD 15 minutes prior to the 24-hour mark and logs AOD values every 30

seconds until 15 minutes after the 24-hour mark. The operator may use this 30-minute window to correct the SPARC's orientation if prior unintended movements took place. The lowest AOD values from the respective measurement sets are taken as the second and third AOD measurements. The flowrate and sampling period may be adjusted depending on the application by changing to a cyclone designed for the desired flowrate and some minor adjustments to the control software.

2.4 Calibration Procedure

One SPARC master unit was calibrated relative to a Cimel CE318 at the Digital Globe AERONET site in Longmont, Colorado [11]. AERONET instruments are either calibrated using the Langely plot technique at Mauna Loa observatory—or relative to other AERONET instruments that have been so calibrated—to AOD uncertainties between 0.002 and 0.005 [33]. The master calibration consisted of co-located and concurrent measurements taken over the course of several hours. The extraterrestrial constant, V_0, was determined for each measurement by solving Equation 2, using the AERONET value for AOD. The extraterrestrial constants for the master unit were then determined by averaging the results of the individual calculations. The extraterrestrial constants with uncertainties (standard error of the mean) for each wavelength of the master unit are given in Table 2.

Table 2. Extraterrestrial constants and uncertainties for the master SPARC unit

Wavelength (nm)	**V_0 (Volts)**
440	0.947 ± 0.004
520	1.368 ± 0.003
680	1.645 ± 0.003
870	1.200 ± 0.001

All other SPARC units were calibrated relative to the to the SPARC master unit by taking a series of simultaneous measurements under variable illumination [12]. The extraterrestrial constant for all non-master units, $V_{0,i}$, was determined as follows [12]:

$$V_{0,i} = V_{0,master} * \rho_i \quad (7)$$

where $V_{0,master}$ is the extraterrestrial constant of the master unit and ρ_i is the average ratio of voltages from uncalibrated unit i to the master unit.

2.5 Co-Location Validation Studies

SPARC AOD measurements were validated in a series of co-location studies using AERONET monitors as the reference method [11]. AERONET monitors were available at two sites along the Colorado Front Range: NEON-CVALLA (N 40º09'39", W 105º10'01") and Digital Globe (N 40º08'20", W 105º08'13"). These tests took place between 3 September and 25 November of 2017 on days with minimal cloud cover. Between two and four calibrated SPARC units were randomly selected on each testing day at set up within 50m of the AERONET monitor. Four-wavelength SPARC AOD measurements were taken manually at five-minute intervals over the course of several hours on each measurement day. These data were then compared with the data published on the online AERONET database [11]. SPARC measurements concurrent within 2 minutes of an AERONET measurement were included in the comparison data set of 130 measurements. The 500 nm and 675 nm AOD values, were adjusted—using Equation 4 and Ångström coefficients from the AERONET data set—to match the 520 nm and 680 nm channels on the SPARC, respectively. The 440 nm and 870 nm channels required no adjustment because both instruments measure at those wavelengths.

To validate the SPARC for gravimetric sampling of $PM_{2.5}$, a series of 48-hr co-locations were conducted using FRM monitors. The FRM consisted of an EPA-certified Louvered Inlet (PM10 – Mesa Labs SSI2.5, Lakewood, CO USA) with an inline $PM_{2.5}$ cyclone (URG Corp 2163, Chapel Hill, NC USA) operating at 16.7 L/min. Co-locations occurred in multiple locations over a 10-week period including downtown Fort Collins, the Colorado State University main campus, and at several personal residences across the city. A custom mount was constructed to support the reference monitors and hold SPARC samplers close to the FRM inlet. A total of 39 paired (48-hr) measurements were collected. A photograph of two SPARC samplers mounted for a $PM_{2.5}$ FRM comparison test is provided in Figure 2-8.

Figure 2-7. Two SPARC samplers mounted with an FRM for a co-location test.

The PMS5003 included in the SPARC was evaluated against a co-located direct-reading FEM monitor (EDM 180, GRIMM, Ainring, Germany) at the main campus of Colorado State University. Two 48-hour tests comprised of hourly readings were conducted for a total of 96 paired measurements. Time-resolved readings from the SPARC PMS5003 were corrected *post hoc*, relative to the SPARC filter, by multiplying each time-resolved reading by a scaling factor equal the ratio of the filter measurement to the 48-hr average of the direct-reading sensor.

CHAPTER 3. RESULTS AND DISCUSSION

3.1 AOD Sensor Evaluation

Close agreement was observed between the SPARC AOD sensors and AERONET monitors. A comparison plot for all wavelengths and all AERONET co-location testing data is provided in Figure 3-1. A Bland-Altman plot for all data is provided in Figure 3-2.

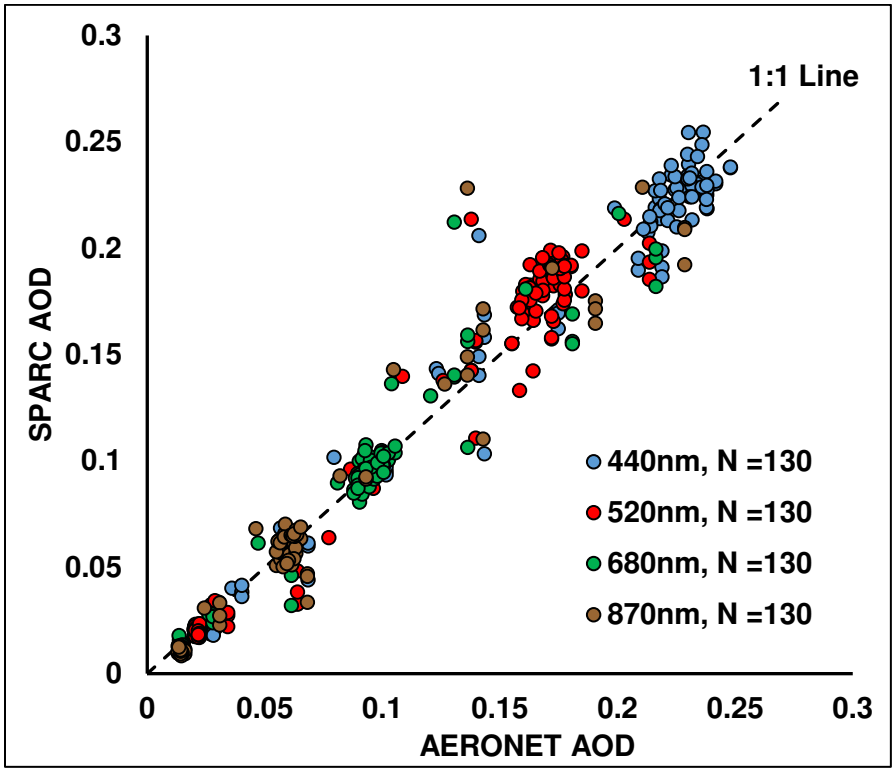

Figure 3-1. AERONET vs SPARC AOD comparison plot. This plot includes all measurements taken across all wavelengths as part of the 2017 co-location campaign.

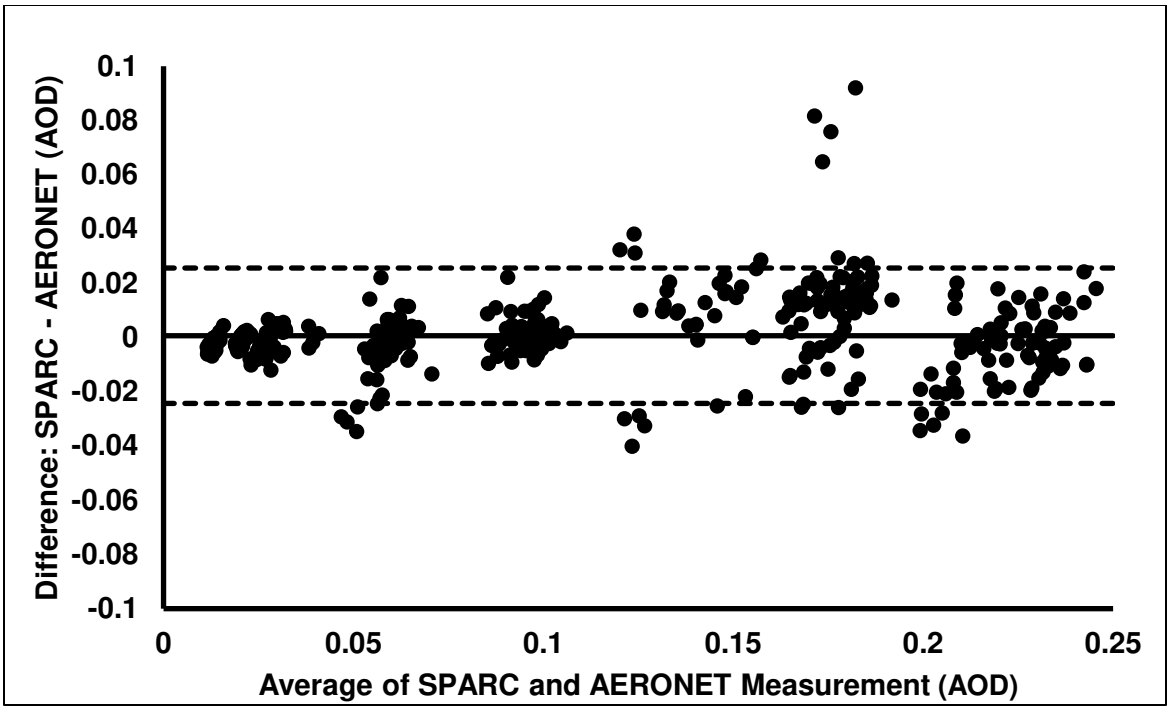

Figure 3-2. AERONET and SPARC AOD Bland-Altman plot. This plot includes all measurements taken across all wavelengths as part of the 2017 co-location campaign. The top and bottom dashed lines represent the upper and lower limits of agreement, respectively, evaluated at 95% confidence. The solid line in between the limits of agreement is the mean difference between the two measurement techniques.

The mean absolute error between the SPARC and AERONET instruments was 0.0079 AOD units (across all wavelengths), yielding a mean relative error of 10%. These deviations are nearly within the published uncertainties of the AERONET monitors [33]. The mean difference calculated from the Bland-Altman plot data was 0.00063 AOD units with upper and lower limits of agreement of 0.026 and -0.024 AOD units, respectively. The Bland-Altman results indicate a low systemic bias between the two instruments in AOD units. These results are encouraging given the relatively low AOD during sampling days, which will tend to magnify error percentages.

The AOD measurement capabilities of the SPARC expand upon those of lower-cost LED Sun photometers. The integrated filtered photodiodes used in the SPARC provide narrower spectral bandwidth readings compared with LEDs. Integrated filtered photodiodes are also available at a greater number of center wavelengths, providing broad wavelength selection over the visible and near-IR spectra. This, coupled with the 4-channel capability of the SPARC, facilitate the evaluation of size distributions from

SPARC data [14]. Computational software make the SPARC AOD calculation process more automated then previous LED photometers. Automation is advantageous because it reduces operator effort and the potential for operator error. LED photometers are advantageous when cost considerations are paramount as material costs saving can be up to 20x over the SPARC [10]. Compared with AERONET monitors, the main advantages of the SPARC are its low cost and portability. The SPARC (including time-resolved and integrated $PM_{2.5}$ monitoring) has a cost of goods 50x lower than the cost of an AERONET CE318 monitor. CE318 monitors are advantageous with respect to measurement automation, the number AOD wavelengths, and the potential for additional sky radiation measurements beyond AOD [11].

AERONET co-location results indicate the SPARC can be used to measure AOD with high accuracy when measurements are prompted and overseen by an operator. However, it remains difficult to assess the reliability of unsupervised measurements taken at 24 and 48-hour intervals after the original measurement. Wind and other disturbances can cause slight misalignment to occur between the first and second measurements. Any software adjustments made to compensate for the day-to-day variation Sun's path assume stability of the instrument throughout the sampling period. Without automated self-correction or operator intervention, misalignment manifests itself with erroneously high AOD measures, which are difficult to discriminate from cloud contaminated measurements. Automated cloud screening requires active solar tracking and relatively high frequency measurements [34]. Manual screening requires operator attention, which cannot be expected for a 48+ hour sampling period. Ongoing work includes the development of an alignment screening method based on measurement from the SPARC solar incidence angle sensor. This sensor is capable of high resolution (<0.05º) incidence angle measurements and can be calibrated relative to the pinhole and target system. Accurate incidence angle calculations will inform the selection of representative AOD measurements taken 24 and 48 hours into the sampling period. The development of a low-cost solar tracking mount is also the subject of ongoing work. Active tracking would eliminate the need for algorithmic adjustments to account for daily solar position, enable measurement of daily AOD trends, increase solar power output, and enable robust cloud screening algorithms.

3.2 Gravimetric $PM_{2.5}$ Sampler Evaluation

Strong agreement was found between the SPARC gravimetric $PM_{2.5}$ and FRM samplers in a co-located study. A comparison plot of SPARC and FRM measurements is provided in Figure 3-3. All fit statistics were evaluated via Deming regression. A Bland-Altman plot for all data is provided in Figure 3-4.

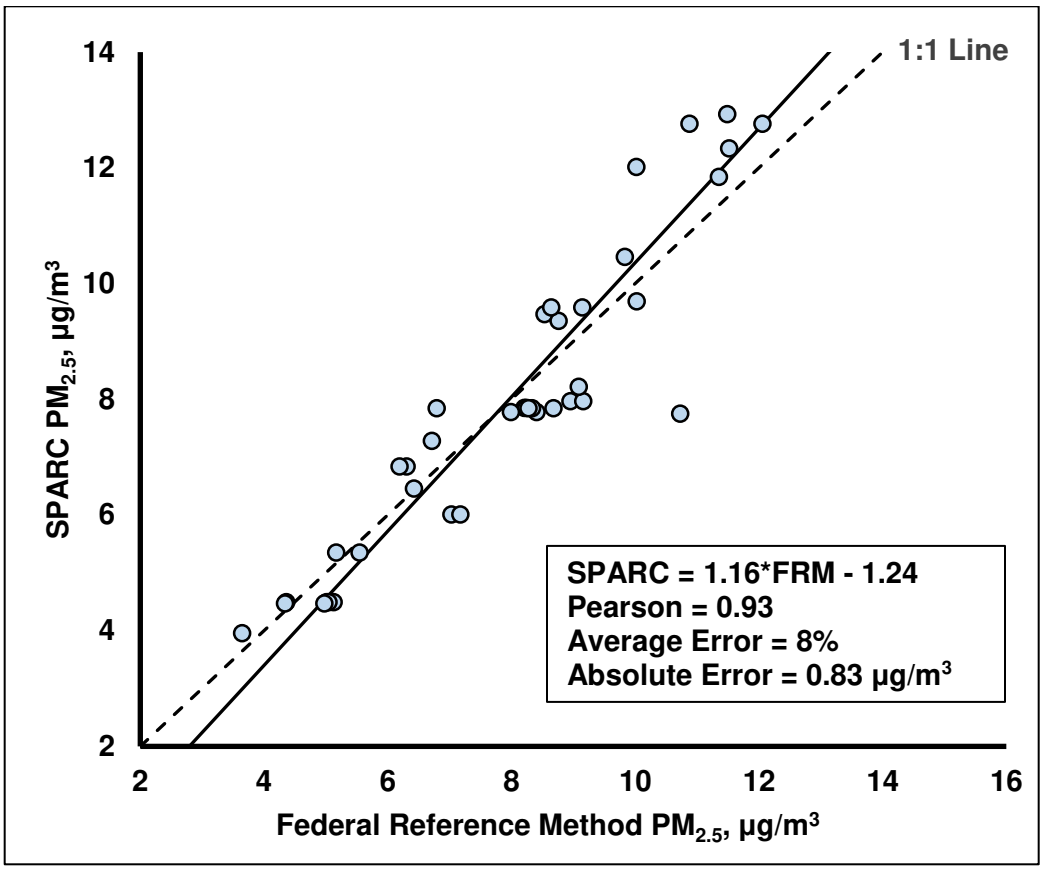

Figure 3-3. FRM $PM_{2.5}$ measurements vs SPARC $PM_{2.5}$ measurements in $\mu g/m^3$. Each data point represents a single 48-hr time-weighted average.

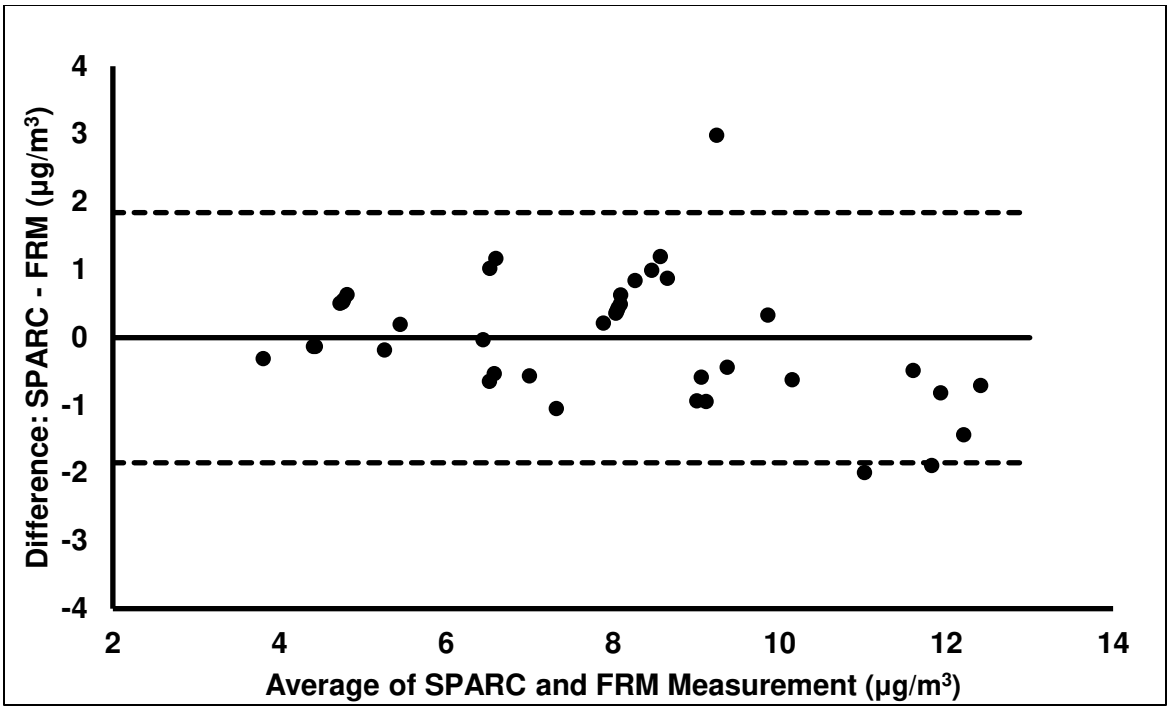

Figure 3-4. FRM and SPARC $PM_{2.5}$ concentration Bland-Altman plot. The top and bottom dashed lines represent the upper and lower limits of agreement, respectively, evaluated at 95% confidence. The solid line in between the limits of agreement is the mean difference between the two measurement techniques.

The Pearson correlation was 0.93 and the mean absolute error was 0.83 µg/m^3 corresponding with a mean relative error of 8%. The relative precision of the SPARC gravimetric $PM_{2.5}$ measurements was 4.9%, expressed as a coefficient of variation among duplicate samplers at the same location. The mean difference calculated from the Bland-Altman plot data was -0.00367 µg/m^3 units with upper and lower limits of agreement of 1.84 and -1.85 µg/m^3 units respectively. The Bland-Altman results indicate a low systemic bias between the two instruments in µg/m^3. These results are encouraging given the low 48-hour average $PM_{2.5}$ concentrations in Fort Collins during this period (ranging from 3.9 to 12.4 µg/m^3). These FRM co-location results are consistent with the agreement observed in previous work [21].

The performance of the SPARC $PM_{2.5}$ sampler is promising in the context of its low cost and compact form factor relative to the FRM. SPARC cost of goods is less than the purchase price of the FRM used in the co-location studies by a factor of 12. The SPARC is also more compact and portable than the FRM. The SPARC is 28 kg lighter, 90 cm shorter, 33 cm narrower and 46 cm shallower than the FRM when both are

in their stowed configuration. Size comparisons when deployed depend on the apparatus used to mount the SPARC (e.g. camera tripod).

3.3 Direct-Reading Sensor Evaluation

Preliminary results for the Plantower direct-reading sensor have been limited but promising. Co-located $PM_{2.5}$ hourly average concentration measurements taken over a 48-hour period are shown in Figure 3-5. A Bland-Altman plot for all data is provided in Figure 3-6.

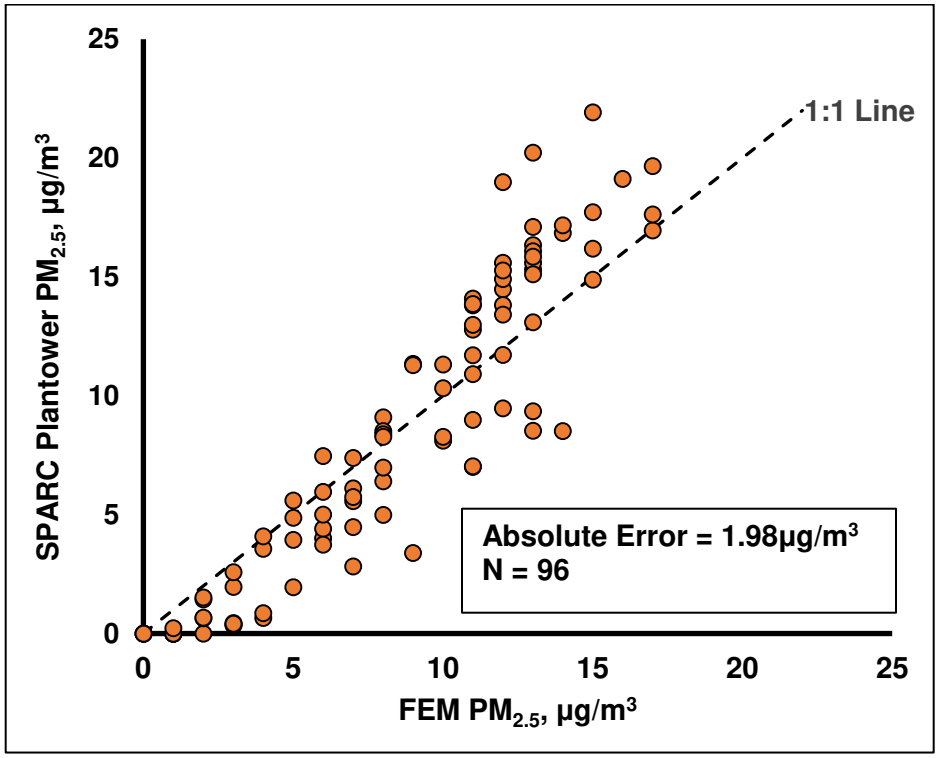

Figure 3-5. Hourly FEM vs Hourly SPARC direct-reading measurements in µg/m^3. The SPARC hourly data were normalized to match the 48-hr gravimetric filter concentration using a mass-scattering coefficient determined in situ.

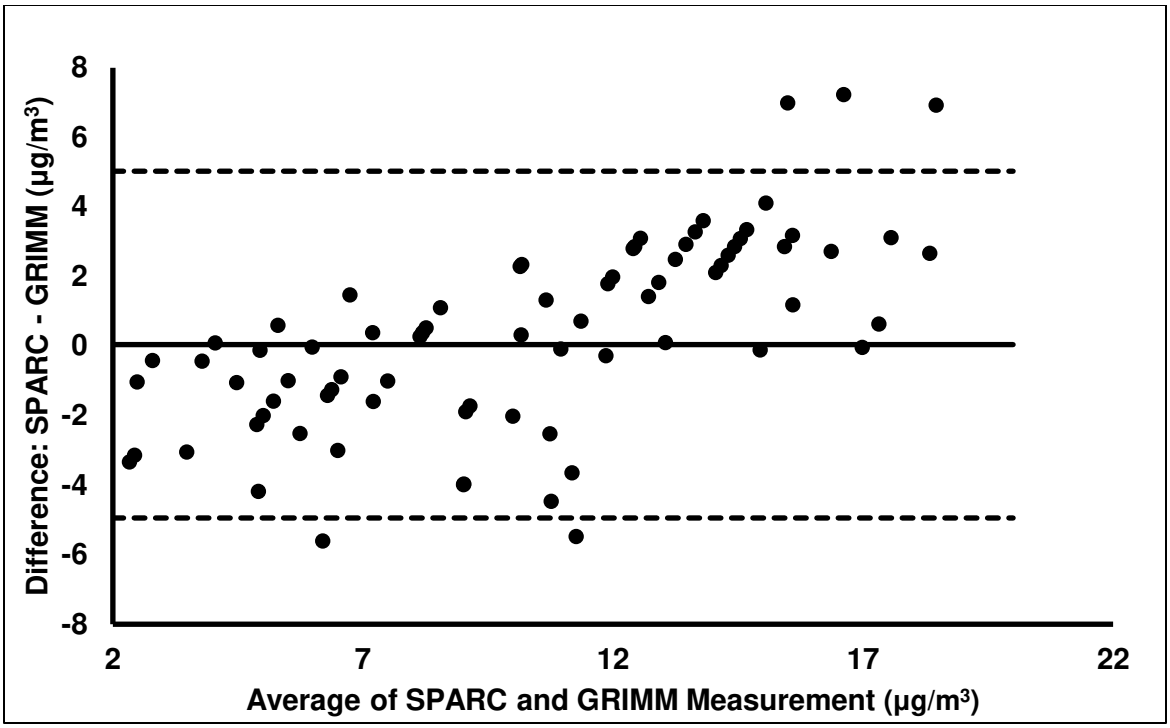

Figure 3-6. GRIMM FEM and SPARC direct-reading $PM_{2.5}$ concentration Bland-Altman plot. The top and bottom dashed lines represent the upper and lower limits of agreement, respectively, evaluated at 95% confidence. The solid line in between the limits of agreement is the mean difference between the two measurement techniques.

An advantage of the SPARC is that gravimetric $PM_{2.5}$ data (i.e., filter mass) can be used to calibrate, in situ, the direct-reading sensor by calculation of a mass-scattering coefficient. This method of calibration may improve the accuracy and precision of measurements from low-cost aerosol nephelometers (such as the Plantower PM5003 used in the SPARC). After normalizing the time-resolved measurements to the filter, the mean absolute error was 1.98 µg/m^3. Concentrations reported by the FEM ranged from 0 to 17 µg/m^3. The mean difference calculated from the Bland-Altman plot data was -0.040 µg/m^3 units with upper and lower limits of agreement of 5.02 and -4.94 µg/m^3 units respectively. These data indicate the SPARC was biased low at low concentrations and biased high at high concentrations.

More data are required to fully evaluate the performance of the direct-reading sensor measurements and the filter normalization technique. One limitation associated the FEM and the PMS5003 is the low resolution. Both monitors report integer values (PMS5003 before filter normalization), which can magnify

or obscure relative errors at low concentrations. Readings of 0 $\mu g/m^3$ are especially problematic because they cannot be corrected to the filter via scaling factor multiplication. This leaves zero readings uncorrected and tends to magnify the scaling of non-zero readings. More testing will be conducted at higher concentrations to limit the effect of resolution on the co-located comparisons.

The SPARC direct-reading sensor represents cost savings over reference-quality direct-reading monitors and performance improvements over low-cost sensors. The cost of goods of the SPARC is 20x less than the purchase prices of two reference quality monitors: the ThermoFisher Tapered Element Oscillating Microbalance (TEOM™) and the GRIMM monitor used in the co-location studies. Filter correction and weatherproof hardware integration may increase the accuracy and durability of the SPARC direct-reading measurement system compared with stand-alone low-cost sensors.

3.4 Wireless Capability

Smartphone connectivity and control is an advantage of the SPARC. The custom SPARC smartphone application serves as a wireless control platform, condensed user manual, and data transfer tool. Wireless control allows the user to start the sampler without the risk of altering an established alignment. Step-by-step instructions reduce the potential for operator error and omission. Wireless data transfer is less labor intensive than hardware alternatives (e.g. SD™ card) and can be directly interfaced with a web server. The present Bluetooth™ smartphone application cannot connect to the SPARC while running, cannot display run data in the app, and downloads data at unsatisfactorily slow speeds (often in excess of five minutes). Expanding the web connectivity of the SPARC using the ESP8266 included on the present version of the device is the subject of ongoing work. Basic data transfer and real-time visualization capabilities have been developed using free Internet of Things (IoT) services and the ESP8266. Further development could enable faster data transfer and immediate feedback for participants in SPARC deployments. These capabilities would bolster the scientific potential of SPARC data and facilitate citizen operator engagement.

3.5 Conclusions

The SPARC is a lightweight and compact alternative to the instruments typically used to sample AOD and $PM_{2.5}$. The SPARC represents a substantial cost saving compared with alternative AOD and $PM_{2.5}$ mass concentration sampling equipment. The small size, durability, increased sampling capabilities and relatively low cost of the SPARC make it a viable option for large scale and spatially dense deployments. Such data sets have the potential facilitate the calibration and validation of satellite-based sensors as they progress toward higher spatial resolution measurement capabilities.

CHAPTER 4. REFERENCES

1. Brauer, M., et al., *Ambient Air Pollution Exposure Estimation for the Global Burden of Disease 2013.* Environ Sci Technol, 2016. **50**(1): p. 79-88.
2. Nel, A., *Air pollution-related illness: effects of particles.* Science, 2005. **35**(29): p. 804-806.
3. Pope, C.A. and D.W. Dockery, *Health Effects of Fine Particulate Air Pollution: Lines that Connect.* Journal of the Air & Waste Management Association, 2006. **56**(6): p. 709-742.
4. de Vroom, J., *The Contribution of Dutch GLOBE Schools to Validation of Aerosol Measurements from Space*, KNMI, Editor. 2004. p. 49.
5. Lv, B., et al., *Improving the Accuracy of Daily PM2.5 Distributions Derived from the Fusion of Ground-Level Measurements with Aerosol Optical Depth Observations, a Case Study in North China.* Environ Sci Technol, 2016. **50**(9): p. 4752-9.
6. van Donkelaar, A., et al., *Global estimates of ambient fine particulate matter concentrations from satellite-based aerosol optical depth: development and application.* Environ Health Perspect, 2010. **118**(6): p. 847-55.
7. van Donkelaar, A., R.V. Martin, and R.J. Park, *Estimating ground-level PM2.5using aerosol optical depth determined from satellite remote sensing.* Journal of Geophysical Research, 2006. **111**(D21).
8. Snider, G., et al., *SPARTAN: a global network to evaluate and enhance satellite-based estimates of ground-level particulate matter for global health applications.* Atmospheric Measurement Techniques, 2015. **8**(1): p. 505-521.
9. Brooks, D.R. and F.M. Mims III, *Development of an inexpensive handheld LED-based Sun photometer for the GLOBE program.* Journal of Geophysical Research, 2001. **106**(D5): p. 4733-4740.
10. Mims III, F.M., *An International Haze-Monitoring Network for Students.* American Meteorological Society, 1999.
11. Holben, B.N., et al., *AERONET - A Federated Instrument Network and Data Archive for Aerosol Characterization.* Remote Sens. Environ., 1998. **66**: p. 1-16.
12. Boersma, K.F. and J.P. de Vroom, *Validation of MODIS aerosol observations over the Netherlands with GLOBE student measurements.* Journal of Geophysical Research, 2006. **111**(D20).
13. Rollin, E.M., *An introduction to the use of Sun-photometry for the atmospheric correction of airborne sensor data*, U.o. Southampton, Editor. 2000.
14. O'Neill, N.T., *Spectral discrimination of coarse and fine mode optical depth.* Journal of Geophysical Research, 2003. **108**(D17).
15. Angstrom, A., *On the Atmospheric Transmission of Sun Radiation and on Dust in the Air.* Geografis Annal, 1929. **2**: p. 156-166.
16. Shaw, G.E., *Sun Photometry.* American Meteorological Society, 1983. **64**(1).
17. Mims III, F.M., *Sun photometer with light-emitting diodes as spectrally selective detectors.* Applied Optics, 1992. **31**(33).
18. Noble, C.A., et al., *Federal Reference and Equivalent Methods for Measuring Fine Particulate Matter.* Aerosol Science and Technology, 2001. **34**(5): p. 457-464.
19. *List of Designated Reference and Equivalent Methods*, E.P. Agency, Editor. 2016.
20. *Ambient Particulat Monitoring, Thermo Fisher Scientific.* [cited 2018; Available from: https://www.thermofisher.com/us/en/home/industrial/environmental/air-quality-analysis/ambient-particulate-monitoring.html.
21. Volckens, J., et al., *Development and evaluation of an ultrasonic personal aerosol sampler.* Indoor Air, 2016.
22. Kelleher, S., et al., *A low-cost PM2.5 monitor for wildland fire smoke.* Atmospheric Measurement Techniques Discussions, 2017: p. 1-19.

23. Murphy, D.M., et al., *A miniature scanning sun photometer for vertical profiles and mobile platforms.* Aerosol Science and Technology, 2015. **50**(1): p. 11-16.
24. Guenter, J. and J. Tatum, *VCSEL Based Optical Sensors*. 2002, Honeywell: Electronic Products. p. 5.
25. Acharya, Y.B., *Spectral and emission characteristics of LED and its application to LED-based sun-photometry.* Optics & Laser Technology, 2005. **37**(7): p. 547-550.
26. Yong, Z., *Digital universal particle concentration sensor*, in *PMS5003 series data manual*. 2016.
27. Torres, B., et al., *Measurements on pointing error and field of view of Cimel-318 Sun photometers in the scope of AERONET.* Atmospheric Measurement Techniques, 2013. **6**(8): p. 2207-2220.
28. Reda, I. and A. Andreas, *Solar Position Algorithm for Solar Radiation Applications*, N.R.E. Laboratory, Editor. 2008.
29. Young, A.T., *Air mass and refraction.* Applied Optics, 1994. **33**(6): p. 3.
30. Bodhaine, B.A., et al., *On Rayleigh Optical Depth Calculations*. Atmospheric and Oceanic Technology, 1999. **16**: p. 8.
31. Van Hueklon, T.K., *Estimating Atmospheric Ozone For Solar Radiation Models.* Solar Energy, 1978. **22**: p. 63-68.
32. Koontz, A., et al., *Aerosol Optical Depth Value-Added Product*, U.S.D.o. Energy, Editor. 2013.
33. Eck, T.F., et al., *Wavelength dependence of the optical depth of biomass burning, urban, and desert dust aerosols.* Journal of Geophysical Research: Atmospheres, 1999. **104**(D24): p. 31333-31349.
34. Smirnov, A., et al., *Cloud-Screening and Quality Control Algorithms for the AERONET Database.* Remote Sens. Environ., 2000. **73**(3): p. 337-349.

APPENDICES

4.1 Additional CAD Images

Figure 5-2. Top view of SPARC housing with solar panel connected.

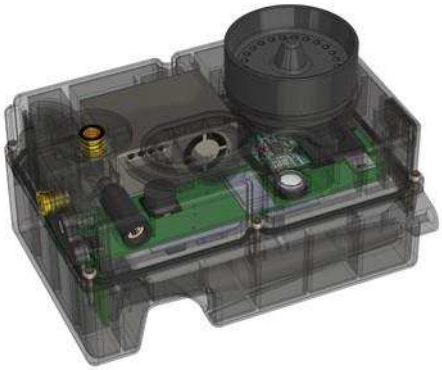

Figure 5-3. Transparent view of SPARC housing.

Figure 5-4. Section view of $PM_{2.5}$ cyclone.

Figure 5-5. CAD design for first generation SPARC.

4.2 Langley Calibration

A Langley calibration was performed during the early stages of device testing to evaluate the extraterrestrial constant according to Equation 3 and to explore the relative behavior of the measurement channel wavelengths. The resulting Langely plot is provided in Figure 5-6.

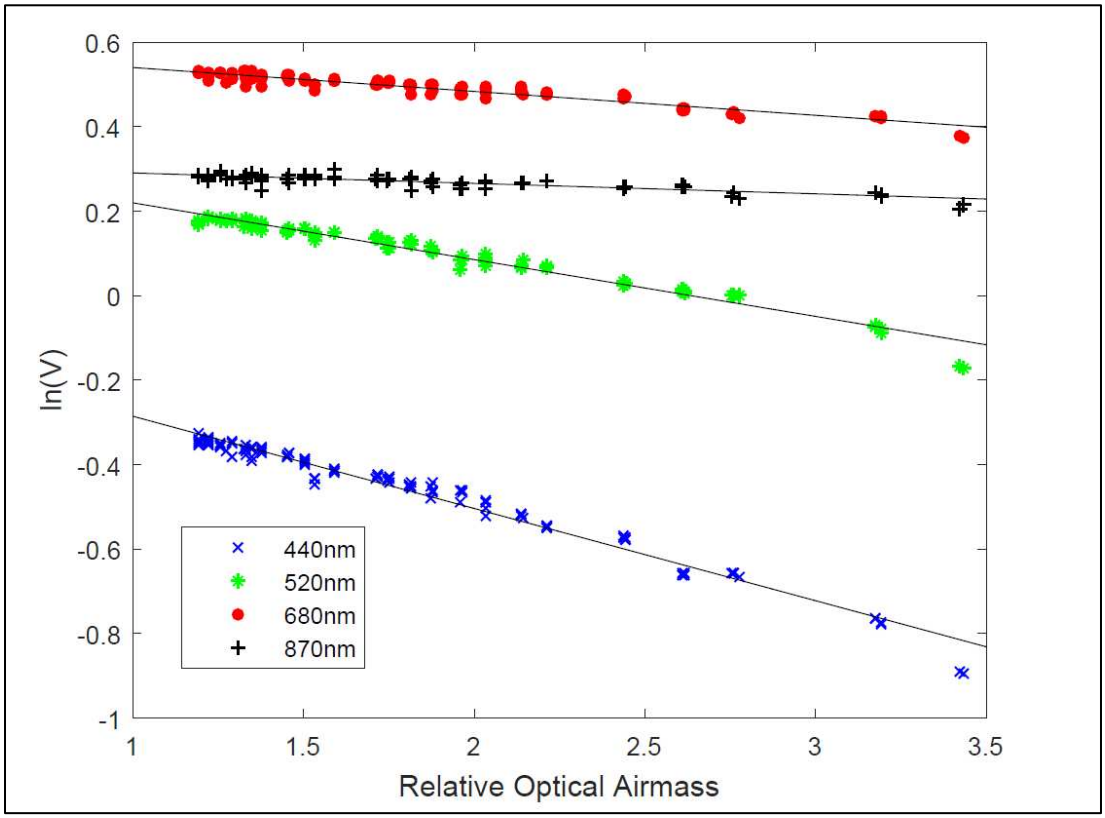

Figure 5-6. Langely calibration results presented for all wavelengths.

The resulting calibration constants were relatively inaccurate compared to those derived from the relative calibration technique and were not used in any device. However, the Langley analysis was instructive for evaluating the AOD measurements from the four channels. According to Equation 3, the optical depth is equal to the slope of the Langley curves. The slope of the Langley curves varied inversely with wavelength, indicating the lower wavelength channels measured higher AOD on this day. This is consistent with established theory regarding wavelength and light attenuation [15].

4.3 Raw Co-Location Data

Table 5-1. Raw Data from SPARC vs. FRM $PM_{2.5}$ filter mass concentration studies.

Date	FRM (ug/m-3)	CEAMS (ug/m-3)	Average	Difference (abs)	Difference (%)	ABS Diff (%)
10/13/2017	7.85202	8.21208	8.03205	0.36006	4.482790819	4.482791
10/13/2017	7.85202	8.23964	8.04583	0.38762	4.817650883	4.817651
10/13/2017	7.77754	8.40498	8.09126	0.62744	7.754540084	7.75454
10/13/2017	7.77754	7.99162	7.88458	0.21408	2.715173161	2.715173
10/17/2017	4.49301	4.36047	4.42674	-0.13254	-2.994076905	2.994077
10/17/2017	4.49301	5.12566	4.809335	0.63265	13.15462533	13.15463
10/17/2017	4.49301	5.01543	4.75422	0.52242	10.98855333	10.98855
10/17/2017	4.49301	5.04299	4.768	0.54998	11.53481544	11.53482
10/23/2017	6.45623	6.42361	6.43992	-0.03262	-0.506528031	0.506528
10/23/2017	6.01097	7.03125	6.52111	1.02028	15.64580263	15.6458
10/23/2017	6.01097	7.17593	6.59345	1.16496	17.66844368	17.66844
11/10/2017	7.28183	6.71296	6.997395	-0.56887	-8.12973971	8.12974
11/10/2017	6.84106	6.30787	6.574465	-0.53319	-8.110013514	8.110014
11/10/2017	6.84106	6.19213	6.516595	-0.64893	-9.958114629	9.958115
11/13/2017	4.47052	4.97685	4.723685	0.50633	10.718962	10.71896
11/13/2017	4.47052	4.34028	4.4054	-0.13024	-2.956371726	2.956372
11/13/2017	3.95623	3.64583	3.80103	-0.3104	-8.166207581	8.166208
11/20/2017	5.34895	5.54395	5.44645	0.195	3.580313782	3.580314
11/20/2017	5.34895	5.16661	5.25778	-0.18234	-3.468003606	3.468004
11/27/2017	7.96852	8.95722	8.46287	0.9887	11.68279792	11.6828
11/27/2017	7.96852	9.16156	8.56504	1.19304	13.92918188	13.92918
11/27/2017	8.21756	9.08851	8.653035	0.87095	10.06525456	10.06525
11/29/2017	10.4615	9.83654	10.14902	-0.62496	-6.157835929	6.157836
11/29/2017	12.3365	11.52153	11.929015	-0.81497	-6.831829786	6.83183
11/29/2017	11.8415	11.35658	11.59904	-0.48492	-4.180690816	4.180691
11/29/2017	9.69321	10.02309	9.85815	0.32988	3.346266794	3.346267
12/1/2017	7.75104	10.73141	9.241225	2.98037	32.2508109	32.25081
12/1/2017	7.84284	6.79332	7.31808	-1.04952	-14.34146661	14.34147
12/1/2017	7.84284	8.33333	8.088085	0.49049	6.064352687	6.064353

12/1/2017	7.84284	8.27546	8.05915	0.43262	5.368059907	5.36806
12/1/2017	7.84284	8.68056	8.2617	0.83772	10.13980174	10.1398
12/6/2017	9.47058	8.53571	9.003145	-0.93487	-10.38381588	10.38382
12/6/2017	9.35294	8.76531	9.059125	-0.58763	-6.486608806	6.486609
12/6/2017	9.58823	8.64286	9.115545	-0.94537	-10.3709652	10.37097
12/6/2017	9.58823	9.14796	9.368095	-0.44027	-4.6996748	4.699675
12/11/2017	12.92646	11.4898	12.20813	-1.43666	-11.76805948	11.76806
12/11/2017	12.01361	10.02037	11.01699	-1.99324	-18.09241907	18.09242
12/22/2017	12.76473	10.87755	11.82114	-1.88718	-15.96445013	15.96445
12/22/2017	12.76473	12.05612	12.410425	-0.70861	-5.709796401	5.709796

Table 5-1. Raw Data from SPARC vs. AERONET co-located AOD studies.

Day	Wavelength (nm)	SPARC AOD	AERONET AOD	Mean (AOD)	Difference (AOD)
3-Sep	440	0.2192	0.2161	0.218	0.0031
3-Sep	440	0.2232	0.2178	0.221	0.0054
3-Sep	440	0.2275	0.2245	0.226	0.003
3-Sep	440	0.2344	0.2229	0.229	0.0115
3-Sep	440	0.2331	0.2365	0.235	-0.0034
3-Sep	440	0.2277	0.2298	0.229	-0.0021
3-Sep	440	0.2395	0.2302	0.235	0.0093
3-Sep	440	0.2311	0.2359	0.234	-0.0048
3-Sep	440	0.2302	0.2341	0.232	-0.0039
3-Sep	440	0.2296	0.2316	0.231	-0.002
3-Sep	440	0.2341	0.23	0.232	0.0041
3-Sep	440	0.2242	0.2308	0.228	-0.0066
3-Sep	440	0.2284	0.2252	0.227	0.0032
3-Sep	440	0.2186	0.2184	0.219	0.0002
3-Sep	440	0.2177	0.2261	0.222	-0.0084
3-Sep	440	0.2139	0.218	0.216	-0.0041
3-Sep	440	0.2184	0.2205	0.219	-0.0021
3-Sep	440	0.2124	0.2142	0.213	-0.0018
3-Sep	440	0.1897	0.2088	0.199	-0.0191
3-Sep	440	0.2112	0.2137	0.212	-0.0025
3-Sep	440	0.213	0.2214	0.217	-0.0084
3-Sep	440	0.2133	0.2317	0.223	-0.0184
3-Sep	440	0.2278	0.238	0.233	-0.0102
3-Sep	440	0.2186	0.2381	0.228	-0.0195
3-Sep	440	0.2192	0.2379	0.229	-0.0187
3-Sep	440	0.2269	0.236	0.231	-0.0091
3-Sep	440	0.2303	0.2418	0.236	-0.0115
3-Sep	440	0.2251	0.238	0.232	-0.0129
3-Sep	440	0.2379	0.248	0.243	-0.0101
3-Sep	440	0.227	0.2161	0.222	0.0109
3-Sep	440	0.2325	0.2178	0.225	0.0147
3-Sep	440	0.2336	0.2245	0.229	0.0091
3-Sep	440	0.2389	0.2229	0.231	0.016
3-Sep	440	0.2545	0.2365	0.246	0.018
3-Sep	440	0.2441	0.2298	0.237	0.0143
3-Sep	440	0.2544	0.2302	0.242	0.0242
3-Sep	440	0.2487	0.2359	0.242	0.0128
3-Sep	440	0.2431	0.2341	0.239	0.009

3-Sep	440	0.2353	0.2316	0.233	0.0037
3-Sep	440	0.2325	0.23	0.231	0.0025
3-Sep	440	0.233	0.2308	0.232	0.0022
3-Sep	440	0.21	0.2252	0.218	-0.0152
3-Sep	440	0.2272	0.2184	0.223	0.0088
3-Sep	440	0.2239	0.2261	0.225	-0.0022
3-Sep	440	0.2177	0.218	0.218	-0.0003
3-Sep	440	0.2208	0.2202	0.221	0.0006
3-Sep	440	0.2074	0.2129	0.21	-0.0055
3-Sep	440	0.2105	0.2142	0.212	-0.0037
3-Sep	440	0.1953	0.2088	0.202	-0.0135
3-Sep	440	0.2089	0.2111	0.21	-0.0022
3-Sep	440	0.2148	0.2137	0.214	0.0011
3-Sep	440	0.219	0.2214	0.22	-0.0024
3-Sep	440	0.2242	0.2317	0.228	-0.0075
3-Sep	440	0.236	0.238	0.237	-0.002
3-Sep	440	0.2275	0.2381	0.233	-0.0106
3-Sep	440	0.2229	0.2379	0.23	-0.015
3-Sep	440	0.2288	0.236	0.232	-0.0072
3-Sep	440	0.2315	0.2418	0.237	-0.0103
3-Sep	440	0.2296	0.238	0.234	-0.0084
18-Nov	440	0.2381	0.248	0.243	-0.0099
18-Nov	440	0.0336	0.0305	0.032	0.0031
18-Nov	440	0.0327	0.0289	0.031	0.0038
18-Nov	440	0.0323	0.0272	0.03	0.0051
18-Nov	440	0.0316	0.0267	0.029	0.0049
18-Nov	440	0.0302	0.0267	0.028	0.0035
18-Nov	440	0.0291	0.0278	0.028	0.0013
18-Nov	440	0.0306	0.0277	0.029	0.0029
18-Nov	440	0.0274	0.0268	0.027	0.0006
18-Nov	440	0.027	0.0272	0.027	-0.0002
18-Nov	440	0.0243	0.0284	0.026	-0.0041
18-Nov	440	0.0256	0.028	0.027	-0.0024
18-Nov	440	0.0246	0.0288	0.027	-0.0042
18-Nov	440	0.0234	0.0286	0.026	-0.0052
18-Nov	440	0.0206	0.0281	0.024	-0.0075
18-Nov	440	0.0324	0.0305	0.031	0.0019
18-Nov	440	0.0334	0.0289	0.031	0.0045
18-Nov	440	0.0312	0.0272	0.029	0.004
18-Nov	440	0.0302	0.0267	0.028	0.0035
18-Nov	440	0.0301	0.0267	0.028	0.0034

18-Nov	440	0.0291	0.0278	0.028	0.0013
18-Nov	440	0.0326	0.0277	0.03	0.0049
18-Nov	440	0.0292	0.0268	0.028	0.0024
18-Nov	440	0.0268	0.0272	0.027	-0.0004
18-Nov	440	0.0275	0.0284	0.028	-0.0009
18-Nov	440	0.0268	0.028	0.027	-0.0012
18-Nov	440	0.027	0.0288	0.028	-0.0018
18-Nov	440	0.0251	0.0286	0.027	-0.0035
18-Nov	440	0.0246	0.0281	0.026	-0.0035
18-Nov	440	0.0239	0.0305	0.027	-0.0066
18-Nov	440	0.0248	0.0289	0.027	-0.0041
18-Nov	440	0.0239	0.0272	0.026	-0.0033
18-Nov	440	0.0244	0.0267	0.026	-0.0023
18-Nov	440	0.0188	0.0267	0.023	-0.0079
18-Nov	440	0.0227	0.0278	0.025	-0.0051
18-Nov	440	0.0223	0.0277	0.025	-0.0054
18-Nov	440	0.0237	0.0268	0.025	-0.0031
18-Nov	440	0.0222	0.0272	0.025	-0.005
18-Nov	440	0.0222	0.0284	0.025	-0.0062
18-Nov	440	0.0208	0.028	0.024	-0.0072
18-Nov	440	0.0212	0.0288	0.025	-0.0076
18-Nov	440	0.0204	0.0286	0.025	-0.0082
25-Nov	440	0.018	0.0281	0.023	-0.0101
25-Nov	440	0.0685	0.0567	0.063	0.0118
25-Nov	440	0.0402	0.0361	0.038	0.0041
25-Nov	440	0.1749	0.1597	0.167	0.0152
25-Nov	440	0.1434	0.123	0.133	0.0204
25-Nov	440	0.1017	0.0795	0.091	0.0222
25-Nov	440	0.1411	0.1239	0.133	0.0172
25-Nov	440	0.2189	0.1988	0.209	0.0201
25-Nov	440	0.0601	0.0685	0.064	-0.0084
25-Nov	440	0.0383	0.0402	0.039	-0.0019
25-Nov	440	0.1711	0.1749	0.173	-0.0038
25-Nov	440	0.1581	0.1434	0.151	0.0147
25-Nov	440	0.0952	0.1017	0.098	-0.0065
25-Nov	440	0.1402	0.1411	0.141	-0.0009
25-Nov	440	0.1911	0.2189	0.205	-0.0278
25-Nov	440	0.0441	0.0685	0.056	-0.0244
25-Nov	440	0.0363	0.0402	0.038	-0.0039
25-Nov	440	0.1622	0.1749	0.169	-0.0127
25-Nov	440	0.1033	0.1434	0.123	-0.0401

25-Nov	440	0.0934	0.1017	0.098	-0.0083
25-Nov	440	0.2059	0.1411	0.174	0.0648
25-Nov	440	0.1987	0.2189	0.209	-0.0202
25-Nov	440	0.0614	0.0685	0.065	-0.0071
25-Nov	440	0.0416	0.0402	0.041	0.0014
25-Nov	440	0.1695	0.1749	0.172	-0.0054
25-Nov	440	0.1687	0.1434	0.156	0.0253
25-Nov	440	0.0974	0.1017	0.1	-0.0043
25-Nov	440	0.1491	0.1411	0.145	0.008
3-Sep	520	0.1866	0.2189	0.203	-0.0323
3-Sep	520	0.1731	0.161	0.167	0.0121
3-Sep	520	0.1827	0.1629	0.173	0.0198
3-Sep	520	0.1835	0.1678	0.176	0.0157
3-Sep	520	0.1854	0.1669	0.176	0.0185
3-Sep	520	0.1932	0.1768	0.185	0.0164
3-Sep	520	0.1827	0.1712	0.177	0.0115
3-Sep	520	0.1939	0.1716	0.183	0.0223
3-Sep	520	0.1872	0.1763	0.182	0.0109
3-Sep	520	0.1886	0.1751	0.182	0.0135
3-Sep	520	0.188	0.1726	0.18	0.0154
3-Sep	520	0.1871	0.172	0.18	0.0151
3-Sep	520	0.1823	0.1728	0.178	0.0095
3-Sep	520	0.1844	0.1683	0.176	0.0161
3-Sep	520	0.1813	0.1629	0.172	0.0184
3-Sep	520	0.1777	0.1682	0.173	0.0095
3-Sep	520	0.1746	0.1626	0.169	0.012
3-Sep	520	0.1661	0.1642	0.165	0.0019
3-Sep	520	0.1695	0.1597	0.165	0.0098
3-Sep	520	0.1551	0.1551	0.155	0
3-Sep	520	0.1668	0.1593	0.163	0.0075
3-Sep	520	0.1704	0.1653	0.168	0.0051
3-Sep	520	0.1656	0.1728	0.169	-0.0072
3-Sep	520	0.1782	0.1779	0.178	0.0003
3-Sep	520	0.1739	0.1769	0.175	-0.003
3-Sep	520	0.1756	0.1774	0.177	-0.0018
3-Sep	520	0.1828	0.1757	0.179	0.0071
3-Sep	520	0.1914	0.1803	0.186	0.0111
3-Sep	520	0.1809	0.1775	0.179	0.0034
3-Sep	520	0.1799	0.1849	0.182	-0.005
3-Sep	520	0.183	0.161	0.172	0.022
3-Sep	520	0.1923	0.1629	0.178	0.0294

3-Sep	520	0.1899	0.1678	0.179	0.0221
3-Sep	520	0.1893	0.1669	0.178	0.0224
3-Sep	520	0.196	0.1768	0.186	0.0192
3-Sep	520	0.1921	0.1712	0.182	0.0209
3-Sep	520	0.199	0.1716	0.185	0.0274
3-Sep	520	0.1943	0.1763	0.185	0.018
3-Sep	520	0.1978	0.1751	0.186	0.0227
3-Sep	520	0.1869	0.1726	0.18	0.0143
3-Sep	520	0.1912	0.172	0.182	0.0192
3-Sep	520	0.1894	0.1728	0.181	0.0166
3-Sep	520	0.1803	0.1683	0.174	0.012
3-Sep	520	0.1755	0.1629	0.169	0.0126
3-Sep	520	0.1955	0.1682	0.182	0.0273
3-Sep	520	0.1815	0.1626	0.172	0.0189
3-Sep	520	0.1423	0.1641	0.153	-0.0218
3-Sep	520	0.1331	0.1584	0.146	-0.0253
3-Sep	520	0.1798	0.1597	0.17	0.0201
3-Sep	520	0.1552	0.1551	0.155	0.0001
3-Sep	520	0.1722	0.1574	0.165	0.0148
3-Sep	520	0.1757	0.1593	0.168	0.0164
3-Sep	520	0.1789	0.1653	0.172	0.0136
3-Sep	520	0.186	0.1728	0.179	0.0132
3-Sep	520	0.1919	0.1779	0.185	0.014
3-Sep	520	0.1885	0.1769	0.183	0.0116
3-Sep	520	0.1865	0.1774	0.182	0.0091
3-Sep	520	0.1904	0.1757	0.183	0.0147
3-Sep	520	0.192	0.1803	0.186	0.0117
3-Sep	520	0.1915	0.1775	0.185	0.014
18-Nov	520	0.1987	0.1849	0.192	0.0138
18-Nov	520	0.0227	0.0224	0.023	0.0003
18-Nov	520	0.0234	0.0217	0.023	0.0017
18-Nov	520	0.0228	0.0206	0.022	0.0022
18-Nov	520	0.0223	0.0202	0.021	0.0021
18-Nov	520	0.0211	0.02	0.021	0.0011
18-Nov	520	0.0211	0.0218	0.021	-0.0007
18-Nov	520	0.0216	0.0205	0.021	0.0011
18-Nov	520	0.0197	0.0208	0.02	-0.0011
18-Nov	520	0.0205	0.0205	0.021	0
18-Nov	520	0.0178	0.0223	0.02	-0.0045
18-Nov	520	0.0191	0.0217	0.02	-0.0026
18-Nov	520	0.0195	0.0222	0.021	-0.0027

18-Nov	520	0.0178	0.0222	0.02	-0.0044
18-Nov	520	0.0179	0.0217	0.02	-0.0038
18-Nov	520	0.0191	0.0224	0.021	-0.0033
18-Nov	520	0.0195	0.0217	0.021	-0.0022
18-Nov	520	0.0175	0.0206	0.019	-0.0031
18-Nov	520	0.0185	0.0202	0.019	-0.0017
18-Nov	520	0.0177	0.02	0.019	-0.0023
18-Nov	520	0.0176	0.0218	0.02	-0.0042
18-Nov	520	0.02	0.0205	0.02	-0.0005
18-Nov	520	0.0189	0.0208	0.02	-0.0019
18-Nov	520	0.0174	0.0205	0.019	-0.0031
18-Nov	520	0.0178	0.0223	0.02	-0.0045
18-Nov	520	0.0175	0.0217	0.02	-0.0042
18-Nov	520	0.0175	0.0222	0.02	-0.0047
18-Nov	520	0.017	0.0222	0.02	-0.0052
18-Nov	520	0.0171	0.0217	0.019	-0.0046
18-Nov	520	0.0233	0.0224	0.023	0.0009
18-Nov	520	0.0221	0.0217	0.022	0.0004
18-Nov	520	0.0232	0.0206	0.022	0.0026
18-Nov	520	0.0218	0.0202	0.021	0.0016
18-Nov	520	0.0205	0.02	0.02	0.0005
18-Nov	520	0.0208	0.0218	0.021	-0.001
18-Nov	520	0.0224	0.0205	0.021	0.0019
18-Nov	520	0.0213	0.0208	0.021	0.0005
18-Nov	520	0.0204	0.0205	0.02	-1E-04
18-Nov	520	0.0235	0.0223	0.023	0.0012
18-Nov	520	0.0201	0.0217	0.021	-0.0016
18-Nov	520	0.019	0.0222	0.021	-0.0032
18-Nov	520	0.018	0.0222	0.02	-0.0042
25-Nov	520	0.0184	0.0217	0.02	-0.0033
25-Nov	520	0.0639	0.0773	0.071	-0.0134
25-Nov	520	0.0343	0.0288	0.032	0.0055
25-Nov	520	0.172	0.1582	0.165	0.0138
25-Nov	520	0.1397	0.1086	0.124	0.0311
25-Nov	520	0.0962	0.0866	0.091	0.0096
25-Nov	520	0.1378	0.1258	0.132	0.012
25-Nov	520	0.2136	0.2029	0.208	0.0107
25-Nov	520	0.0483	0.0639	0.056	-0.0156
25-Nov	520	0.0274	0.0343	0.031	-0.0069
25-Nov	520	0.168	0.172	0.17	-0.004
25-Nov	520	0.1559	0.1397	0.148	0.0162

25-Nov	520	0.0927	0.0962	0.094	-0.0035
25-Nov	520	0.1426	0.1378	0.14	0.0048
25-Nov	520	0.1934	0.2136	0.204	-0.0202
25-Nov	520	0.0327	0.0639	0.048	-0.0312
25-Nov	520	0.0287	0.0343	0.032	-0.0056
25-Nov	520	0.1574	0.172	0.165	-0.0146
25-Nov	520	0.1108	0.1397	0.125	-0.0289
25-Nov	520	0.0926	0.0962	0.094	-0.0036
25-Nov	520	0.2136	0.1378	0.176	0.0758
25-Nov	520	0.2023	0.2136	0.208	-0.0113
25-Nov	520	0.0383	0.0639	0.051	-0.0256
25-Nov	520	0.0222	0.0343	0.028	-0.0121
25-Nov	520	0.158	0.172	0.165	-0.014
25-Nov	520	0.1566	0.1397	0.148	0.0169
25-Nov	520	0.0871	0.0962	0.092	-0.0091
25-Nov	520	0.1424	0.1378	0.14	0.0046
3-Sep	680	0.1854	0.2136	0.2	-0.0282
3-Sep	680	0.0807	0.0903	0.086	-0.0096
3-Sep	680	0.0844	0.0914	0.088	-0.007
3-Sep	680	0.0879	0.0944	0.091	-0.0065
3-Sep	680	0.0917	0.0943	0.093	-0.0026
3-Sep	680	0.0985	0.1001	0.099	-0.0016
3-Sep	680	0.0924	0.0964	0.094	-0.004
3-Sep	680	0.0989	0.0965	0.098	0.0024
3-Sep	680	0.0998	0.1002	0.1	-0.0004
3-Sep	680	0.1006	0.0997	0.1	0.0009
3-Sep	680	0.0973	0.0978	0.098	-0.0005
3-Sep	680	0.0995	0.0975	0.099	0.002
3-Sep	680	0.0975	0.0978	0.098	-0.0003
3-Sep	680	0.0976	0.095	0.096	0.0026
3-Sep	680	0.0938	0.092	0.093	0.0018
3-Sep	680	0.1018	0.0952	0.099	0.0066
3-Sep	680	0.1027	0.0922	0.097	0.0105
3-Sep	680	0.1076	0.093	0.1	0.0146
3-Sep	680	0.0999	0.0902	0.095	0.0097
3-Sep	680	0.0865	0.0879	0.087	-0.0014
3-Sep	680	0.0925	0.0902	0.091	0.0023
3-Sep	680	0.094	0.0931	0.094	0.0009
3-Sep	680	0.0943	0.098	0.096	-0.0037
3-Sep	680	0.1022	0.1009	0.102	0.0013
3-Sep	680	0.0992	0.1002	0.1	-0.001

3-Sep	680	0.098	0.1005	0.099	-0.0025
3-Sep	680	0.0995	0.0994	0.099	0.0001
3-Sep	680	0.1003	0.1026	0.101	-0.0023
3-Sep	680	0.098	0.1006	0.099	-0.0026
3-Sep	680	0.1038	0.1054	0.105	-0.0016
3-Sep	680	0.0903	0.0903	0.09	0
3-Sep	680	0.1011	0.0914	0.096	0.0097
3-Sep	680	0.094	0.0944	0.094	-0.0004
3-Sep	680	0.0933	0.0943	0.094	-0.001
3-Sep	680	0.0961	0.1001	0.098	-0.004
3-Sep	680	0.0915	0.0964	0.094	-0.0049
3-Sep	680	0.0998	0.0965	0.098	0.0033
3-Sep	680	0.0981	0.1002	0.099	-0.0021
3-Sep	680	0.1048	0.0997	0.102	0.0051
3-Sep	680	0.0947	0.0978	0.096	-0.0031
3-Sep	680	0.0974	0.0975	0.097	-0.0001
3-Sep	680	0.0929	0.0978	0.095	-0.0049
3-Sep	680	0.1003	0.095	0.098	0.0053
3-Sep	680	0.0932	0.092	0.093	0.0012
3-Sep	680	0.0971	0.0952	0.096	0.0019
3-Sep	680	0.0962	0.0922	0.094	0.004
3-Sep	680	0.1048	0.0926	0.099	0.0122
3-Sep	680	0.094	0.0895	0.092	0.0045
3-Sep	680	0.0935	0.0902	0.092	0.0033
3-Sep	680	0.0849	0.0879	0.086	-0.003
3-Sep	680	0.0919	0.0886	0.09	0.0033
3-Sep	680	0.0923	0.0902	0.091	0.0021
3-Sep	680	0.0964	0.0931	0.095	0.0033
3-Sep	680	0.0992	0.098	0.099	0.0012
3-Sep	680	0.103	0.1009	0.102	0.0021
3-Sep	680	0.1039	0.1002	0.102	0.0037
3-Sep	680	0.0947	0.1005	0.098	-0.0058
3-Sep	680	0.1037	0.0994	0.102	0.0043
3-Sep	680	0.1037	0.1026	0.103	0.0011
3-Sep	680	0.1022	0.1006	0.101	0.0016
18-Nov	680	0.107	0.1054	0.106	0.0016
18-Nov	680	0.0144	0.0153	0.015	-0.0009
18-Nov	680	0.0145	0.0139	0.014	0.0006
18-Nov	680	0.0147	0.0139	0.014	0.0008
18-Nov	680	0.014	0.0137	0.014	0.0003
18-Nov	680	0.0135	0.014	0.014	-0.0005

18-Nov	680	0.014	0.0142	0.014	-0.0002
18-Nov	680	0.0141	0.0137	0.014	0.0004
18-Nov	680	0.0134	0.0136	0.014	-0.0002
18-Nov	680	0.0139	0.0137	0.014	0.0002
18-Nov	680	0.0129	0.015	0.014	-0.0021
18-Nov	680	0.0135	0.0139	0.014	-0.0004
18-Nov	680	0.0144	0.0146	0.015	-0.0002
18-Nov	680	0.0133	0.0146	0.014	-0.0013
18-Nov	680	0.0121	0.014	0.013	-0.0019
18-Nov	680	0.0124	0.0153	0.014	-0.0029
18-Nov	680	0.0127	0.0139	0.013	-0.0012
18-Nov	680	0.0131	0.0139	0.014	-0.0008
18-Nov	680	0.0125	0.0137	0.013	-0.0012
18-Nov	680	0.0112	0.014	0.013	-0.0028
18-Nov	680	0.0131	0.0142	0.014	-0.0011
18-Nov	680	0.013	0.0137	0.013	-0.0007
18-Nov	680	0.0132	0.0136	0.013	-0.0004
18-Nov	680	0.0124	0.0137	0.013	-0.0013
18-Nov	680	0.0124	0.015	0.014	-0.0026
18-Nov	680	0.0129	0.0139	0.013	-0.001
18-Nov	680	0.0124	0.0146	0.014	-0.0022
18-Nov	680	0.0122	0.0146	0.013	-0.0024
18-Nov	680	0.0118	0.014	0.013	-0.0022
18-Nov	680	0.014	0.0153	0.015	-0.0013
18-Nov	680	0.0127	0.0139	0.013	-0.0012
18-Nov	680	0.0144	0.0139	0.014	0.0005
18-Nov	680	0.0134	0.0137	0.014	-0.0003
18-Nov	680	0.0122	0.014	0.013	-0.0018
18-Nov	680	0.0127	0.0142	0.013	-0.0015
18-Nov	680	0.0158	0.0137	0.015	0.0021
18-Nov	680	0.0179	0.0136	0.016	0.0043
18-Nov	680	0.0127	0.0137	0.013	-0.001
18-Nov	680	0.0136	0.015	0.014	-0.0014
18-Nov	680	0.0129	0.0139	0.013	-0.001
18-Nov	680	0.0122	0.0146	0.013	-0.0024
18-Nov	680	0.0124	0.0146	0.014	-0.0022
25-Nov	680	0.0127	0.014	0.013	-0.0013
25-Nov	680	0.0614	0.0472	0.054	0.0142
25-Nov	680	0.028	0.0262	0.027	0.0018
25-Nov	680	0.1808	0.161	0.171	0.0198
25-Nov	680	0.1363	0.104	0.12	0.0323

25-Nov	680	0.0896	0.0809	0.085	0.0087
25-Nov	680	0.1306	0.1206	0.126	0.01
25-Nov	680	0.2163	0.2006	0.208	0.0157
25-Nov	680	0.0515	0.0614	0.056	-0.0099
25-Nov	680	0.0279	0.028	0.028	-1E-04
25-Nov	680	0.1691	0.1808	0.175	-0.0117
25-Nov	680	0.1562	0.1363	0.146	0.0199
25-Nov	680	0.092	0.0896	0.091	0.0024
25-Nov	680	0.1395	0.1306	0.135	0.0089
25-Nov	680	0.1955	0.2163	0.206	-0.0208
25-Nov	680	0.0321	0.0614	0.047	-0.0293
25-Nov	680	0.0239	0.028	0.026	-0.0041
25-Nov	680	0.1561	0.1808	0.168	-0.0247
25-Nov	680	0.1063	0.1363	0.121	-0.03
25-Nov	680	0.0886	0.0896	0.089	-0.001
25-Nov	680	0.2122	0.1306	0.171	0.0816
25-Nov	680	0.1996	0.2163	0.208	-0.0167
25-Nov	680	0.0462	0.0614	0.054	-0.0152
25-Nov	680	0.0268	0.028	0.027	-0.0012
25-Nov	680	0.1551	0.1808	0.168	-0.0257
25-Nov	680	0.1592	0.1363	0.148	0.0229
25-Nov	680	0.0871	0.0896	0.088	-0.0025
25-Nov	680	0.1404	0.1306	0.136	0.0098
3-Sep	870	0.182	0.2163	0.199	-0.0343
3-Sep	870	0.0572	0.0568	0.057	0.0004
3-Sep	870	0.0579	0.0568	0.057	0.0011
3-Sep	870	0.0581	0.0593	0.059	-0.0012
3-Sep	870	0.0613	0.0595	0.06	0.0018
3-Sep	870	0.0633	0.0631	0.063	0.0002
3-Sep	870	0.0623	0.06	0.061	0.0023
3-Sep	870	0.0607	0.0605	0.061	0.0002
3-Sep	870	0.0623	0.0633	0.063	-0.001
3-Sep	870	0.0629	0.0631	0.063	-0.0002
3-Sep	870	0.0604	0.0615	0.061	-0.0011
3-Sep	870	0.0613	0.0615	0.061	-0.0002
3-Sep	870	0.0607	0.0625	0.062	-0.0018
3-Sep	870	0.0595	0.0602	0.06	-0.0007
3-Sep	870	0.0576	0.0578	0.058	-0.0002
3-Sep	870	0.0581	0.0594	0.059	-0.0013
3-Sep	870	0.0574	0.0585	0.058	-0.0011
3-Sep	870	0.0606	0.0589	0.06	0.0017

3-Sep	870	0.057	0.0568	0.057	0.0002
3-Sep	870	0.0508	0.055	0.053	-0.0042
3-Sep	870	0.0571	0.0566	0.057	0.0005
3-Sep	870	0.0576	0.0584	0.058	-0.0008
3-Sep	870	0.059	0.0612	0.06	-0.0022
3-Sep	870	0.0623	0.0633	0.063	-0.001
3-Sep	870	0.0598	0.0624	0.061	-0.0026
3-Sep	870	0.0602	0.0628	0.062	-0.0026
3-Sep	870	0.0611	0.0619	0.062	-0.0008
3-Sep	870	0.0615	0.0637	0.063	-0.0022
3-Sep	870	0.0611	0.0624	0.062	-0.0013
3-Sep	870	0.0635	0.0653	0.064	-0.0018
3-Sep	870	0.0538	0.0568	0.055	-0.003
3-Sep	870	0.0568	0.0568	0.057	0
3-Sep	870	0.0526	0.0593	0.056	-0.0067
3-Sep	870	0.0542	0.0595	0.057	-0.0053
3-Sep	870	0.059	0.0631	0.061	-0.0041
3-Sep	870	0.0542	0.06	0.057	-0.0058
3-Sep	870	0.056	0.0605	0.058	-0.0045
3-Sep	870	0.0566	0.0633	0.06	-0.0067
3-Sep	870	0.0591	0.0631	0.061	-0.004
3-Sep	870	0.0523	0.0615	0.057	-0.0092
3-Sep	870	0.0512	0.0615	0.056	-0.0103
3-Sep	870	0.054	0.0625	0.058	-0.0085
3-Sep	870	0.0532	0.0602	0.057	-0.007
3-Sep	870	0.0503	0.0578	0.054	-0.0075
3-Sep	870	0.0517	0.0594	0.056	-0.0077
3-Sep	870	0.0657	0.0585	0.062	0.0072
3-Sep	870	0.0702	0.0588	0.065	0.0114
3-Sep	870	0.0626	0.056	0.059	0.0066
3-Sep	870	0.0629	0.0568	0.06	0.0061
3-Sep	870	0.0574	0.055	0.056	0.0024
3-Sep	870	0.0622	0.0556	0.059	0.0066
3-Sep	870	0.0616	0.0566	0.059	0.005
3-Sep	870	0.0642	0.0584	0.061	0.0058
3-Sep	870	0.0652	0.0612	0.063	0.004
3-Sep	870	0.0674	0.0633	0.065	0.0041
3-Sep	870	0.0655	0.0624	0.064	0.0031
3-Sep	870	0.0645	0.0628	0.064	0.0017
3-Sep	870	0.0649	0.0619	0.063	0.003
3-Sep	870	0.0655	0.0637	0.065	0.0018

3-Sep	870	0.0657	0.0624	0.064	0.0033
18-Nov	870	0.0689	0.0653	0.067	0.0036
18-Nov	870	0.0114	0.0161	0.014	-0.0047
18-Nov	870	0.0124	0.0148	0.014	-0.0024
18-Nov	870	0.0126	0.0142	0.013	-0.0016
18-Nov	870	0.0119	0.0146	0.013	-0.0027
18-Nov	870	0.0109	0.0144	0.013	-0.0035
18-Nov	870	0.0124	0.0146	0.014	-0.0022
18-Nov	870	0.0128	0.0136	0.013	-0.0008
18-Nov	870	0.0118	0.014	0.013	-0.0022
18-Nov	870	0.013	0.0132	0.013	-0.0002
18-Nov	870	0.012	0.0148	0.013	-0.0028
18-Nov	870	0.0113	0.0143	0.013	-0.003
18-Nov	870	0.0129	0.0143	0.014	-0.0014
18-Nov	870	0.0125	0.0143	0.013	-0.0018
18-Nov	870	0.0116	0.0134	0.013	-0.0018
18-Nov	870	0.0093	0.0161	0.013	-0.0068
18-Nov	870	0.01	0.0148	0.012	-0.0048
18-Nov	870	0.0096	0.0142	0.012	-0.0046
18-Nov	870	0.0108	0.0146	0.013	-0.0038
18-Nov	870	0.0088	0.0144	0.012	-0.0056
18-Nov	870	0.0094	0.0146	0.012	-0.0052
18-Nov	870	0.0105	0.0136	0.012	-0.0031
18-Nov	870	0.0103	0.014	0.012	-0.0037
18-Nov	870	0.0097	0.0132	0.011	-0.0035
18-Nov	870	0.0108	0.0148	0.013	-0.004
18-Nov	870	0.0114	0.0143	0.013	-0.0029
18-Nov	870	0.0118	0.0143	0.013	-0.0025
18-Nov	870	0.0109	0.0143	0.013	-0.0034
18-Nov	870	0.011	0.0134	0.012	-0.0024
18-Nov	870	0.0108	0.0161	0.013	-0.0053
18-Nov	870	0.0098	0.0148	0.012	-0.005
18-Nov	870	0.0104	0.0142	0.012	-0.0038
18-Nov	870	0.0102	0.0146	0.012	-0.0044
18-Nov	870	0.0098	0.0144	0.012	-0.0046
18-Nov	870	0.0085	0.0146	0.012	-0.0061
18-Nov	870	0.0106	0.0136	0.012	-0.003
18-Nov	870	0.0109	0.014	0.012	-0.0031
18-Nov	870	0.0106	0.0132	0.012	-0.0026
18-Nov	870	0.01	0.0148	0.012	-0.0048
18-Nov	870	0.0094	0.0143	0.012	-0.0049

18-Nov	870	0.0105	0.0143	0.012	-0.0038
18-Nov	870	0.0111	0.0143	0.013	-0.0032
25-Nov	870	0.0125	0.0134	0.013	-0.0009
25-Nov	870	0.0682	0.0462	0.057	0.022
25-Nov	870	0.0309	0.0243	0.028	0.0066
25-Nov	870	0.1906	0.1723	0.181	0.0183
25-Nov	870	0.1429	0.1048	0.124	0.0381
25-Nov	870	0.093	0.082	0.088	0.011
25-Nov	870	0.1362	0.1266	0.131	0.0096
25-Nov	870	0.2286	0.2107	0.22	0.0179
25-Nov	870	0.0469	0.0682	0.058	-0.0213
25-Nov	870	0.0229	0.0309	0.027	-0.008
25-Nov	870	0.1752	0.1906	0.183	-0.0154
25-Nov	870	0.1615	0.1429	0.152	0.0186
25-Nov	870	0.0919	0.093	0.092	-0.0011
25-Nov	870	0.1404	0.1362	0.138	0.0042
25-Nov	870	0.2097	0.2286	0.219	-0.0189
25-Nov	870	0.0335	0.0682	0.051	-0.0347
25-Nov	870	0.0333	0.0309	0.032	0.0024
25-Nov	870	0.1648	0.1906	0.178	-0.0258
25-Nov	870	0.1103	0.1429	0.127	-0.0326
25-Nov	870	0.0914	0.093	0.092	-0.0016
25-Nov	870	0.2282	0.1362	0.182	0.092
25-Nov	870	0.2088	0.2286	0.219	-0.0198
25-Nov	870	0.0458	0.0682	0.057	-0.0224
25-Nov	870	0.0273	0.0309	0.029	-0.0036
25-Nov	870	0.1715	0.1906	0.181	-0.0191
25-Nov	870	0.1715	0.1429	0.157	0.0286
25-Nov	870	0.0926	0.093	0.093	-0.0004
25-Nov	870	0.149	0.1362	0.143	0.0128
25-Nov	870	0.1922	0.2286	0.21	-0.0364

Table 5-2. Raw Data from SPARC vs. FEM direct-reading $PM_{2.5}$ co-location studies

Date and Time (MST)	GRIMM ($\mu g/m^3$)	SPARC ($\mu g/m^3$)	Average ($\mu g/m^3$)	Difference ($\mu g/m^3$)
11/20/2017 13:00	2	0	1	-2
11/20/2017 14:00	2	0.648247431	1.324123716	-1.351752569
11/20/2017 15:00	4	0.664453617	2.332226809	-3.335546383
11/20/2017 16:00	4	0.858927847	2.429463924	-3.141072153
11/20/2017 17:00	3	0.437567016	1.718783508	-2.562432984
11/20/2017 18:00	3	0.367703375	1.683851688	-2.632296625
11/20/2017 19:00	3	1.969051573	2.484525787	-1.030948427
11/20/2017 20:00	3	0.356536087	1.678268044	-2.643463913
11/20/2017 21:00	3	0.42136083	1.710680415	-2.57863917
11/20/2017 22:00	1	0	0.5	-1
11/20/2017 23:00	1	0	0.5	-1
11/21/2017 0:00	1	0	0.5	-1
11/21/2017 1:00	1	0	0.5	-1
11/21/2017 2:00	1	0	0.5	-1
11/21/2017 3:00	0	0	0	0
11/21/2017 4:00	0	0	0	0
11/21/2017 5:00	0	0	0	0
11/21/2017 6:00	0	0	0	0
11/21/2017 7:00	1	0	0.5	-1
11/21/2017 8:00	1	0.228793211	0.614396606	-0.771206789
11/21/2017 9:00	2	0.678208447	1.339104224	-1.321791553
11/21/2017 10:00	2	1.442350535	1.721175268	-0.557649465
11/21/2017 11:00	2	1.523381464	1.761690732	-0.476618536
11/21/2017 12:00	3	2.582094811	2.791047406	-0.417905189
11/21/2017 13:00	4	3.562637144	3.781318572	-0.437362856
11/21/2017 14:00	4	4.09206191	4.046030955	0.09206191
11/21/2017 15:00	5	4.878061921	4.939030961	-0.121938079
11/21/2017 16:00	5	5.599237188	5.299618594	0.599237188
11/21/2017 17:00	6	7.471051646	6.735525823	1.471051646
11/21/2017 18:00	9	11.34433005	10.17216503	2.34433005
11/21/2017 19:00	10	10.32334034	10.16167017	0.32334034
11/21/2017 20:00	11	13.80767029	12.40383515	2.80767029
11/21/2017 21:00	14	16.85443321	15.42721661	2.85443321
11/21/2017 22:00	16	19.1205755	17.56028775	3.1205755
11/21/2017 23:00	17	19.66350542	18.33175271	2.66350542
11/22/2017 0:00	17	16.96338236	16.98169118	-0.03661764
11/22/2017 1:00	15	14.88538164	14.94269082	-0.11461836

11/22/2017 2:00	12	14.48833009	13.24416505	2.48833009
11/22/2017 3:00	12	13.82387647	12.91193824	1.82387647
11/22/2017 4:00	13	15.31484557	14.15742279	2.31484557
11/22/2017 5:00	12	15.60655691	13.80327846	3.60655691
11/22/2017 6:00	13	15.60655691	14.30327846	2.60655691
11/22/2017 7:00	13	17.11373219	15.0568661	4.11373219
11/22/2017 8:00	14	17.17855693	15.58927847	3.17855693
11/22/2017 9:00	13	16.34393836	14.67196918	3.34393836
11/22/2017 10:00	11	12.78668058	11.89334029	1.78668058
11/22/2017 11:00	10	8.111195985	9.055597993	-1.888804015
11/22/2017 12:00	5	1.95497778	3.47748889	-3.04502222
12/1/2017 15:00	7	2.819878729	4.909939365	-4.180121271
12/1/2017 16:00	9	3.393608772	6.196804386	-5.606391228
12/1/2017 17:00	8	4.995087069	6.497543535	-3.004912931
12/1/2017 18:00	11	7.016000158	9.008000079	-3.983999842
12/1/2017 19:00	13	8.531684974	10.76584249	-4.468315026
12/1/2017 20:00	14	8.522152366	11.26107618	-5.477847634
12/1/2017 21:00	13	9.351489341	11.17574467	-3.648510659
12/1/2017 22:00	11	8.985094962	9.992547481	-2.014905038
12/1/2017 23:00	12	9.475413257	10.73770663	-2.524586743
12/2/2017 0:00	10	8.274304534	9.137152267	-1.725695466
12/2/2017 1:00	13	16.09104384	14.54552192	3.09104384
12/2/2017 2:00	17	17.63532648	17.31766324	0.63532648
12/2/2017 3:00	11	7.035065376	9.017532688	-3.964934624
12/2/2017 4:00	6	4.003695742	5.001847871	-1.996304258
12/2/2017 5:00	6	4.413597925	5.206798963	-1.586402075
12/2/2017 6:00	6	3.746315302	4.873157651	-2.253684698
12/2/2017 7:00	5	3.946500089	4.473250045	-1.053499911
12/2/2017 8:00	6	5.967413178	5.983706589	-0.032586822
12/2/2017 9:00	8	6.405913188	7.202956594	-1.594086812
12/2/2017 10:00	7	4.480326188	5.740163094	-2.519673812
12/2/2017 11:00	6	5.004619678	5.502309839	-0.995380322
12/2/2017 12:00	7	6.113686656	6.556843328	-0.886313344
12/2/2017 13:00	7	5.576576212	6.288288106	-1.423423788
12/2/2017 14:00	7	5.748163173	6.374081587	-1.251836827
12/2/2017 15:00	8	6.989502736	7.494751368	-1.010497264
12/2/2017 16:00	8	9.103641509	8.551820755	1.103641509
12/2/2017 17:00	11	12.98341334	11.99170667	1.98341334
12/2/2017 18:00	13	15.86226123	14.43113062	2.86226123
12/2/2017 19:00	15	16.18636993	15.59318497	1.18636993
12/2/2017 20:00	13	13.09780464	13.04890232	0.09780464

12/2/2017 21:00	12	13.42191335	12.71095668	1.42191335
12/2/2017 22:00	11	14.09872858	12.54936429	3.09872858
12/2/2017 23:00	13	15.10918512	14.05459256	2.10918512
12/3/2017 0:00	12	14.91853294	13.45926647	2.91853294
12/3/2017 1:00	12	15.28077208	13.64038604	3.28077208
12/3/2017 2:00	13	20.22819611	16.61409806	7.22819611
12/3/2017 3:00	15	21.92500049	18.46250025	6.92500049
12/3/2017 4:00	15	17.72095839	16.3604792	2.72095839
12/3/2017 5:00	12	18.98895695	15.49447848	6.98895695
12/3/2017 6:00	11	10.9148372	10.9574186	-0.0851628
12/3/2017 7:00	8	8.522152366	8.261076183	0.522152366
12/3/2017 8:00	7	7.387771905	7.193885953	0.387771905
12/3/2017 9:00	8	8.379163232	8.189581616	0.379163232
12/3/2017 10:00	8	8.274304534	8.137152267	0.274304534
12/3/2017 11:00	9	11.28660895	10.14330448	2.28660895
12/3/2017 12:00	10	11.32473939	10.6623697	1.32473939
12/3/2017 13:00	11	11.71557635	11.35778818	0.71557635
12/3/2017 14:00	11	13.86041336	12.43020668	2.86041336
12/3/2017 15:00	12	11.71737982	11.85868991	-0.28262018

4.4 AOD Sensor Circuit Schematic

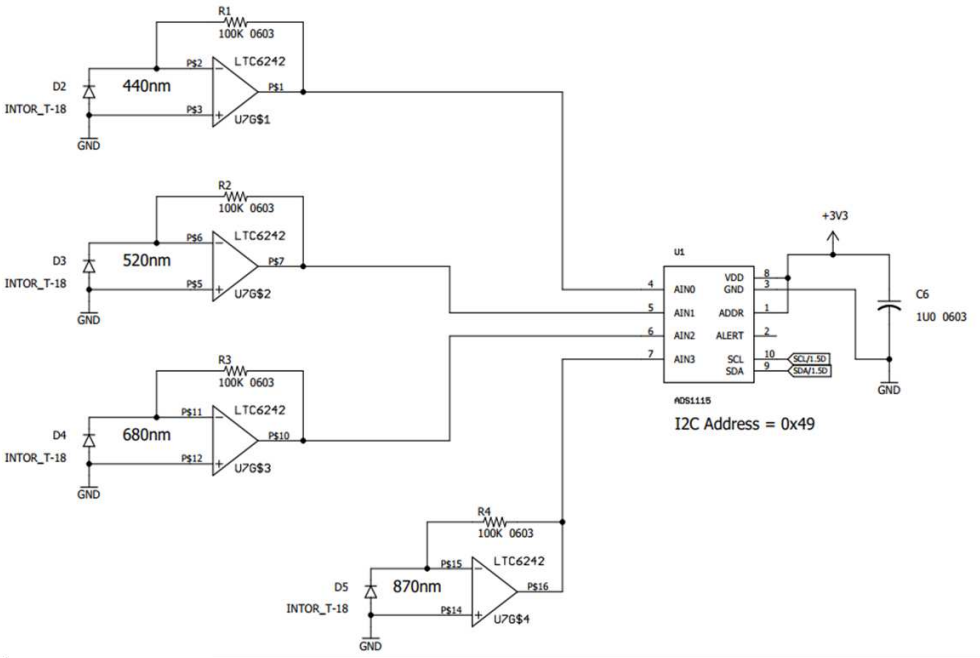

Figure 5-6. Schematic for AOD sensor circuitry. A transimpedence circuit was implemented for each channel with a 100k gain resistor.